AIAA SciTech Forum
8–12 January 2018, Kissimmee, Florida
2018 AIAA/ASCE/AHS/ASC Structures, Structural Dynamics, and Materials Conference

10.2514/6.2018-0412

Aerodynamic Shape Optimisation of Benchmark Problems Using SU2

Guangda Yang[*] and Andrea Da Ronch[†]

Faculty of Engineering and the Environment
University of Southampton, Southampton, SO17 1BJ, UK

In this paper, results are presented from the application of an open–source code, SU2, to a suite of benchmark cases defined by the AIAA Aerodynamic Design Optimisation Discussion Group. Two geometry parameterisation methods are employed, which are Hicks–Henne bump functions and Free–Form Deformation. Mesh deformation is achieved by solving linear elasticity equations. The adjoint solver within SU2 enables efficient sensitivity analysis, and gradient–based optimisation is performed using the SLSQP optimiser. The first optimisation problem studied is the drag minimisation of the NACA 0012 aerofoil in inviscid, transonic flow subject to a minimum thickness constraint. The shock wave is greatly weakened and moved downstream, achieving as much as 83% drag reduction. The second is the lift–constrained drag minimisation of the RAE 2822 aerofoil in transonic, viscous flow. The shock is eliminated, reducing drag by 38%. The NACA 0012 optimisation shows sensitivity to several numerical settings in the parameterisation approaches, whereas the RAE 2822 optimisation is insensitive to those parameter settings. The same pattern is also observed in the design variable dimensionality study. Moreover, for both two–dimensional optimisation problems, non–unique flow solutions exist on the optimised aerofoil. The third problem is the twist optimisation of a rectangular wing to minimise the induced drag at fixed lift in subsonic, inviscid flow. A nearly elliptical lift distribution is obtained using Free–Form Deformation twist parameterisation. The drag is reduced by approximately 1 count and an improved span efficiency is achieved.

I.   Introduction

There is growing concern over the environmental impact of aviation carbon emissions in the past few years. Great efforts have been made by aircraft designers to achieve fuel burn reduction when designing new aircraft. The uncertainty of jet fuel prices also puts pressure on aircraft manufacturers to develop more energy efficient aircraft technologies. To this end, one key aspect is to improve aerodynamic performance through drag minimisation using Computational Fluid Dynamics (CFD). With the recent rapid development of computer technology, numerical optimisation has shown the potential to be a powerful tool in fulfilling such tasks effectively and efficiently. By integrating a CFD solver with an optimisation algorithm, geometry parameterisation and mesh deformation tools, designers are able to perform Aerodynamic Shape Optimisation (ASO) with ease. A robust ASO framework allows not only exploiting the design space for traditional tube–and–wing type aircraft configurations, but also exploring unconventional configurations that can result in dramatic improvement of the aerodynamic performance.

The AIAA Aerodynamic Design Optimisation Discussion Group (ADODG)[a] has established a set of benchmark problems with increasing complexity, ranging from a single–point aerofoil optimisation case to a multi–point wing–body–tail optimisation case. The purpose is to provide benchmark test cases among the research community for exercising aerodynamic optimisation methods. A number of research groups from both industry and academia have tested their codes and presented their results, highlighting the contributions of their approach. A variety of methods and tools have been used for each component of the

---

[*]PhD Student. Email: Guangda.Yang@soton.ac.uk
[†]Lecturer, AIAA Senior Member. Email: A.Da-Ronch@soton.ac.uk
[a]https://info.aiaa.org/tac/ASG/APATC/AeroDesignOpt-DG/default.aspx

American Institute of Aeronautics and Astronautics

ASO framework. For example, methods of choice for the geometry parameterisation were B–splines,[1–3] Bézier curve,[2,4] Free–Form Deformation (FFD),[3] Hicks–Henne bump functions,[5,6] Radial Basis Functions (RBFs)[7,8] and Singular Value Decomposition (SVD),[8,9] among others. Reference[10] selected six parameterisation methods and investigated their impact on the optimisation results. The choice of both the flow solver and the optimisation algorithm has also shown influence on the optimisation results. In Refs.,[11,12] a cross–analysis on the optimised geometries obtained from several institutions was carried out.

The open–source SU2 code[13,14] has been recently developed to perform Partial Differential Equation (PDE) analysis and solve PDE–constrained optimisation problems. The feature of high–fidelity flow and adjoint analysis as well as the capability of modules coupling to perform complex tasks has made SU2 a powerful suite. In this paper, the SU2 framework is used to perform gradient–based ASO for three ADODG benchmark cases. The first optimisation case studied is the drag minimisation of the NACA 0012 aerofoil in transonic, inviscid flow, with a minimum thickness constraint. The second case is the drag minimisation of the RAE 2822 aerofoil in transonic, viscous flow, subject to lift, pitching moment and area constraints. The third case is the twist optimisation of a rectangular wing in subsonic, inviscid flow, subject to a lift constraint.

The aim of this paper is to establish the sensitivity of the optimal aerodynamic shape on a number of model parameters, which have been largely neglected to date. The work is built around three technical objectives. First, two parameterisation methods are used to manipulate geometry changes, and their impact on the results is investigated for two aerofoil problems. The second objective is to establish the robustness of the optimal results (from Objective 1) to changes on numerical settings used in the parameterisation methods. The last objective revisits the optimal solution for increasing number of the design variables, and this is carried out for both aerofoils and a finite–span wing.

The paper continues in Section II with a description of the methods and algorithms employed in this work. Then, Section III discusses the three ADODG benchmark problems and presents the optimisation results. Finally, conclusions and future work are summarised in Section IV.

II.   Methodology

This Section briefly overviews the methods and algorithms employed for the results presented in this paper. In particular, the Section is organised in four parts: the optimisation framework within SU2 in II.A, the governing equations for the flow and adjoint solvers in II.B, the geometry parameterisation methods and the mesh deformation strategy in II.C, and the gradient evaluation approach in II.D.

A.   Optimisation Framework

One of the key features of SU2 is that each software module is designed for specific functionality and can be executed individually. By coupling multiple modules and then integrating with an optimisation package, SU2 is able to solve design optimisation problems. A typical design process for aerodynamic optimisation is illustrated in Figure 1. A baseline geometry and mesh are taken as input to the design cycle, along with a chosen objective function (J) to evaluate optimisation performance and a vector of design variables ($\vec{x}$) to parameterise the shape. A gradient–based optimiser is then enabled to drive the design cycle, and the iterative design loop will proceed until the optimisation convergence criterion is satisfied. Several primary modules that are called by the optimiser in the design loop are introduced as follows:

- SU2_CFD - performs flow and adjoint analysis by solving governing PDE equations.

- SU2_DEF - perturbs the geometry surface and deforms the surrounding volume mesh given a set of design variables in the optimisation process.

- SU2_DOT - computes the gradient by projecting the adjoint surface sensitivity into the design space through a dot product operation.

When the gradient of the objective function (∇J) is obtained, the Sequential Quadratic Programming (SQP) optimisation algorithm is employed to guide the search for optimum design. In this work, the Sequential Least SQuares Programming (SLSQP) optimiser is used, which is implemented in the open–source SciPy library and is the default optimiser for SU2. To determine the convergence of optimisation, the Karush–Kuhn–Tucker (KKT) condition[15,16] is met within the desired tolerance (e.g. $1 \cdot 10^{-6}$). Additionally, the design process will be terminated if the number of design iterations exceeds a specified value (e.g. 100).
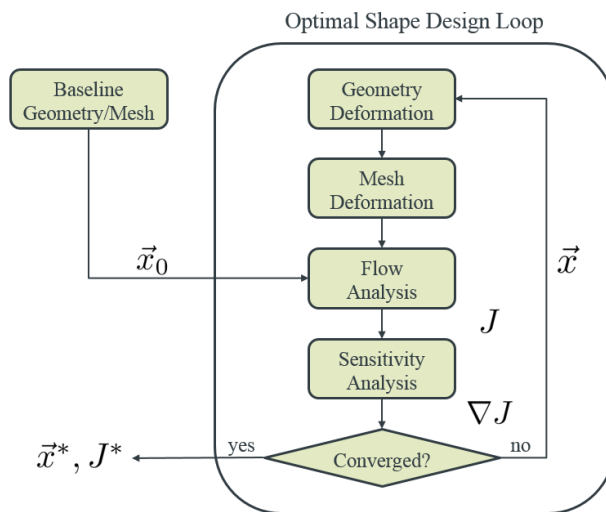
American Institute of Aeronautics and Astronautics

Figure 1. Flow chart for gradient–based shape optimisation within SU2.

B.   Flow and Adjoint Solver

The SU2_CFD module within SU2 is able to solve multiple physical models, of which the PDE systems can be generalised in the same form. In this work, the flow around aerodynamic bodies are governed by compressible Euler or Reynolds–Averaged Navier–Stokes (RANS) equations. Following the general notation presented in Refs.,[13, 14] the RANS equations are formulated as

$$\frac{\partial \mathbf{U}}{\partial t} + \nabla \cdot \mathbf{F}^c - \nabla \cdot \mathbf{F}^v - \mathbf{Q} = \mathbf{R} = 0 \tag{1}$$

where $\mathbf{U}$ represents the vector of conservative variables, $\mathbf{F}^c$ and $\mathbf{F}^v$ are convective and viscous fluxes, respectively, $\mathbf{Q}$ is a generic source term and $\mathbf{R}$ represents the numerical residual for the equations. By setting the terms $\mathbf{Q}$ and $\mathbf{F}^v$ to zero, the Euler equations are recovered.

The governing equations are numerically solved using a finite volume method (FVM). The Jameson–Schmidt–Turkel (JST)[17] scheme is used for the spatial discretisation in this work. The solution is marched in time using an implicit Euler scheme until a steady state is reached. For RANS simulations, the classical one–equation Spalart–Allmaras (SA)[18] turbulence model is used to close the system of equations.

In terms of adjoint solver, both continuous and discrete adjoint method have been implemented in SU2, and the continuous adjoint approach is employed in this work. Again, following the notation in Refs.,[13, 14] the adjoint RANS equations are given by

$$-\frac{\partial \mathbf{\Psi}}{\partial t} - \nabla \mathbf{\Psi} \cdot \left[\left(\frac{\partial \mathbf{F}^c}{\partial \mathbf{U}} \right)_i - \mu_{tot} \left(\frac{\partial \mathbf{F}^v}{\partial \mathbf{U}} \right)_i \right] - \nabla \cdot \left[\nabla \mathbf{\Psi} \cdot \mu_{tot} \frac{\partial}{\partial x_j} \left(\frac{\partial \mathbf{F}^v}{\partial \mathbf{U}} \right)_i \right] - \mathbf{\Psi} \frac{\partial \mathbf{Q}}{\partial \mathbf{U}} = 0 \tag{2}$$

where $\mathbf{\Psi}$ are the adjoint variables that correspond to each of the conserved variables in the flow problem, μ_{tot} is the sum of dynamic viscosity and turbulent viscosity, and $i, j = 1, 2, 3$. The adjoint Euler equations can be easily obtained by removing the corresponding viscous and source terms. The numerical discretisation and solution of Eq. (2) follow the methods for solving Eq. (1). The reader is referred to Ref.[19] for more details.

C.   Geometry Parameterisation and Mesh Deformation

The shape parameterisation and mesh deformation play an important role in an ASO framework and must be robust and efficient enough for the design process. Two commonly–used parameterisation methods have been implemented in SU2 and are employed in this work, which correspond to Hicks–Henne bump functions and FFD. After perturbing the geometry surface with a chosen parameterisation, the SU2_DEF module deforms the volume mesh using a technique based on the linear elasticity equations.[20]

American Institute of Aeronautics and Astronautics

1. Hicks–Henne Bump Functions

Hicks and Henne[21] introduced an analytical approach that takes a baseline geometry and adds a linear combination of bump functions to the upper and lower surface to create a new shape. For two–dimensional (2D) problems, the parameterised geometry function can be expressed by:

$$
\begin{cases}
y = y_{\text{baseline}} + \sum_{i=1}^{n} b_i(x) \\
b_i(x) = a_i \left[\sin\left(\pi x^{\frac{\log 0.5}{\log h_i}} \right) \right]^{t_i}, \quad 0 \leq x \leq 1
\end{cases}
\tag{3}
$$

where n is the number of bump functions; $b_i(x)$ is the bump function (or basis function) proposed by Hicks and Henne; a_i represents the maximum bump amplitude and acts as the weighting coefficient; h_i locates the maximum point of the bump and t_i controls the width of the bump. By setting all the coefficients a_i to zero, the baseline geometry is recovered.

By inspecting Eq. (3), it is apparent that every bump function is defined by three parameters that can either be fixed or varying during optimisation. To ensure the parameterisation is a linear function of the design variables, only the bump amplitude coefficients a_i are allowed to vary and thus treated as design variables, while the other two parameters are fixed. For the bump maximum positions h_i, two approaches are employed in this study: a) even distribution over the range of $[0.5/n, \, 1 - 0.5/n]$; and b) uneven distribution described by a "one–minus–cosine" function:

$$
h_i = \frac{1}{2} \left[1 - \cos\left(\frac{i\pi}{n+1} \right) \right], \quad i = 1, \ldots, n.
\tag{4}
$$

A comparison of these two distributions is shown in Figure 2, where a set of ten bump functions are distributed on the NACA 0012 aerofoil. It is not unexpected that the "one–minus–cosine" distribution results in bump functions clustered at the leading edge (LE) and trailing edge (TE) of the aerofoil.


(a) Even distribution

(b) "One–minus–cosine" distribution
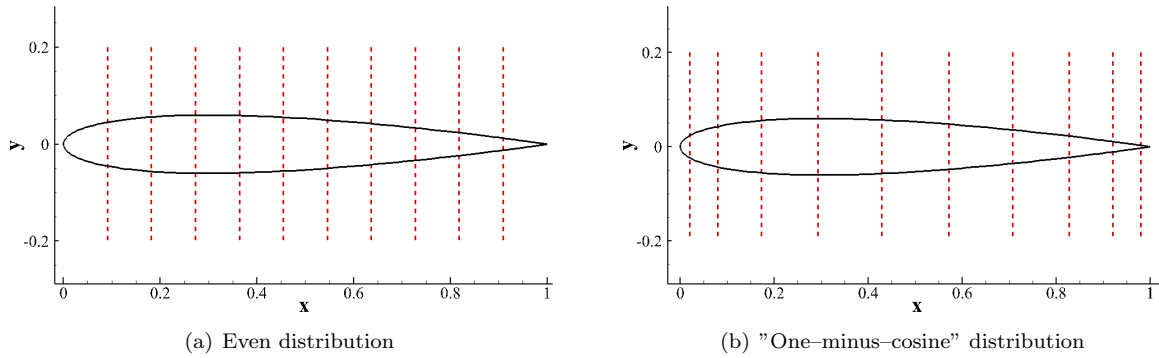
Figure 2. Two distributions for Hicks–Henne bump functions ($n = 10$) on the NACA 0012 aerofoil. Red dashed lines indicate bump maximum positions.

For the bump width control parameter, t, a constant value is specified within the SU2 code. In this study, in addition to the default setting $t = 3$, a range of values of t is defined and the impact on the optimisation results is investigated. Figure 3 shows three sets of Hicks–Henne bump functions with different settings of t. It is observed that the bump width narrows down as t increases, which indicates that a relatively smaller value of t can provide more global shape control whereas a relatively larger value of t generates more local shape control.

2. Free–Form Deformation

Free–Form Deformation (FFD), which was initially proposed by Sederberg and Parry,[22] is taken as the second parameterisation method in this paper. The basic FFD concept can be visualised by embedding a flexible object inside a flexible volume and deforming both of them simultaneously by perturbing the lattice

American Institute of Aeronautics and Astronautics

(a) $t = 1$ (b) $t = 3$ (c) $t = 10$
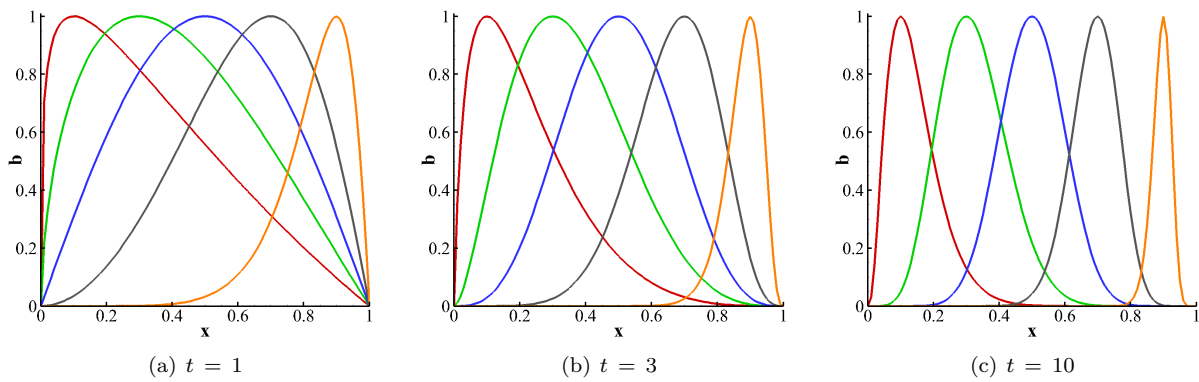
Figure 3. Three sets of Hicks–Henne bump functions with different settings of t ($n = 5$, $a_i = 1$, $h_i \in [0.1, 0.9]$).

of the volume. The FFD control volume (or FFD box) has a topology of a cube when deforming three–dimensional (3D) objects or a rectangular plane for 2D objects, and thus it can be parameterised as either a trivariate volume or a bivariate surface. Both Bézier curves and uniform B–splines are available in SU2 as FFD blending function, and the former is used in this study. Figure 4 illustrates the FFD box encapsulating a rectangular wing and the RAE 2822 aerofoil, where a lattice of control points are uniformly spaced on the surface of FFD box.

(a) Rectangular wing   (b) RAE 2822 aerofoil
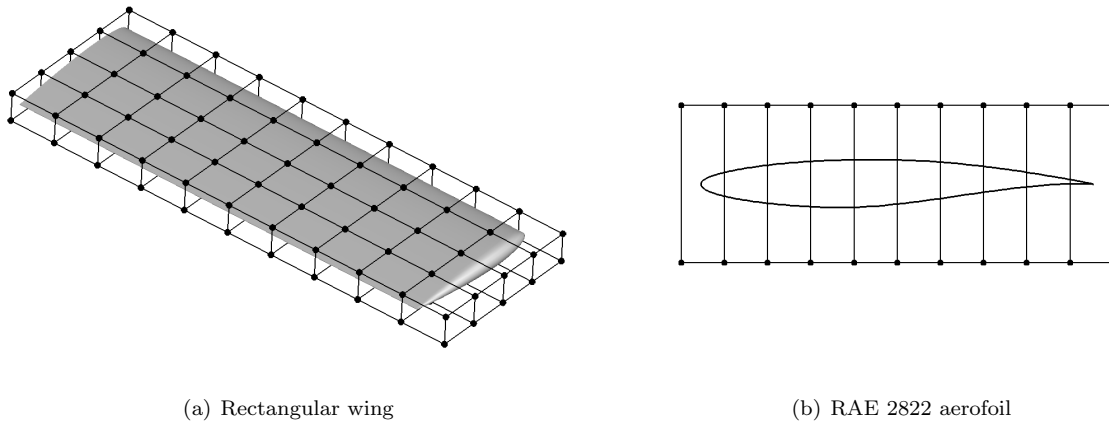
Figure 4. View of FFD box enclosing the embedded object, including the control points shown in spheres.

The parameterised Bézier volume can be described using the following equation:

$$\mathbf{X}(\xi, \eta, \zeta) = \sum_{i=0}^{l} \sum_{j=0}^{m} \sum_{k=0}^{n} \mathbf{P}_{i,j,k} \, B_i^l(\xi) \, B_j^m(\eta) \, B_k^n(\zeta) \tag{5}$$

where l, m, n are the degrees of FFD blending function; ξ, η, $\zeta \in [0, 1]$ are the parametric coordinates; $\mathbf{P}_{i,j,k}$ are the Cartesian coordinates of the control point (i, j, k); $\mathbf{X}$ are the corresponding Cartesian coordinates (x, y, z) for a given (ξ, η, ζ) in the Bézier volume; $B_i^l(\xi)$, $B_j^m(\eta)$, and $B_k^n(\zeta)$ are the Bernstein polynomials, which are expressed as

$$\begin{cases} B_i^l(\xi) = \dfrac{l!}{i!\,(l-i)!} \, \xi^i (1-\xi)^{l-i} \\[2mm] B_j^m(\eta) = \dfrac{m!}{j!\,(m-j)!} \, \eta^j (1-\eta)^{m-j} \\[2mm] B_k^n(\zeta) = \dfrac{n!}{k!\,(n-k)!} \, \zeta^k (1-\zeta)^{n-k} \end{cases} \tag{6}$$

American Institute of Aeronautics and Astronautics

The control points of the FFD box are defined as the design variables, the number of which depends on the degree of the chosen Bernstein polynomials.

FFD is numerically executed in three steps. Firstly, for the embedded object, a mapping is performed from the physical space to the parametric space of the FFD box. The parametric coordinates (ξ, η, ζ) of each surface mesh node are determined and remain unchanged during the optimisation. Note that this mapping is evaluated only once. Secondly, the FFD control points are perturbed, which leads to the deformation of the FFD box as well as the embedded object. Thirdly, once the FFD box has been deformed, the new Cartesian coordinates $\mathbf{X} = (x, y, z)$ of the embedded object in physical space are algebraically computed using Eq. (5).

A key feature of FFD parameterisation approach is that multiple control points can be grouped together to perform specific motions and thus achieve desired shape deformation, such as redefining aerofoil camber and thickness, applying changes to wing twist and sweep, etc.

3. Mesh Deformation

At each design step of the aerodynamic optimisation, the computational mesh needs to be recomputed. Mesh regeneration is often time–consuming and may often introduce additional discretisation errors. Hence, the strategy of mesh deformation with high efficiency and robustness is preferred. The mesh deformation method employed in SU2 code models the computational mesh as an elastic solid using the equations of linear elasticity.[14, 20] The modulus of elasticity in each mesh cell may be treated in three ways: a) inversely proportional to the cell volume; b) inversely proportional to the distance from the wall; and c) being a constant value. In this study, the first option is employed and thereby the mesh quality in boundary layers and regions of high resolution is preserved. More details on the mesh deformation method may be found in Ref.[20]

D. Gradient Evaluation

In gradient–based optimisation, it is necessary to evaluate the gradient accurately and efficiently in each design step to establish a new search direction for the optimiser. Within SU2 framework, the calculation of the gradient can be formulated in the following equation:

$$
\underbrace{\begin{bmatrix} \frac{\partial f}{\partial x_1} \\ \frac{\partial f}{\partial x_2} \\ \vdots \\ \frac{\partial f}{\partial x_n} \end{bmatrix}}_{\text{Gradients}} = \underbrace{\begin{bmatrix} \frac{\partial s_1}{\partial x_1} & \cdots & \frac{\partial s_m}{\partial x_1} \\ \vdots & \ddots & \vdots \\ \frac{\partial s_1}{\partial x_n} & \cdots & \frac{\partial s_m}{\partial x_n} \end{bmatrix}}_{\text{Geometric Sensitivities}} \underbrace{\begin{bmatrix} \frac{\partial f}{\partial s_1} \\ \frac{\partial f}{\partial s_2} \\ \vdots \\ \frac{\partial f}{\partial s_m} \end{bmatrix}}_{\text{Surface Sensitivities}}
\tag{7}
$$

where n and m are the number of design variables and surface mesh nodes, respectively; f represents the function of interest, being the objective or constraint function; x_i $(i = 1, 2, \ldots, n)$ are the design variables; the variables s_j $(j = 1, 2, \ldots, m)$ represent the local surface normal displacements for each discrete mesh node on the geometry surface.

The term $\partial f/\partial \mathbf{s}$ is called the surface sensitivities, which represent the variation of the function of interest with respect to infinitesimal perturbations of the geometry shape in local surface normal direction. The surface sensitivities at each mesh node are computed by solving only once the adjoint equations, of which the computational cost is in the order of one flow solution. The Jacobian matrix $\partial \mathbf{s}/\partial \mathbf{x}$ is known as the geometric sensitivities, which measure the influence of change of design variables on the positions of surface mesh nodes. The geometric sensitivities are calculated using finite difference method, of which the computational expense is negligible as it does not require the solution of governing PDE equations. The gradients $\partial f/\partial \mathbf{x}$ are then computed by the SU2_DOT module through a dot product operation between the geometric and surface sensitivities. The computational cost of evaluating gradients using the adjoint approach is independent of the number of design variables but dependent on the number of functions of interest, which provides great efficiency in practical design problems.

III.   Results

In this Section, results are presented for three ADODG benchmark optimisation cases. For each case, the optimisation problem is firstly introduced, followed by the description of geometry and grid. The optimisation results are then provided in detail. Lastly, a summary is included for both aerofoil optimisation cases.

A.   Case 1: Drag Minimisation of the NACA 0012 Aerofoil in Transonic Inviscid Flow

1.   Problem Description

The optimisation problem is the drag minimisation of a modified NACA 0012 aerofoil in inviscid, transonic flow. The freestream Mach number, M, is 0.85, and the angle of attack, α, is fixed at 0 degree. The thickness is constrained to be greater than or equal to the initial aerofoil thickness along the entire chord. The optimisation problem is written as

$$\text{Minimise:} \quad C_d$$
$$\text{Subject to:} \quad y \geq y_{baseline}, \, \forall \, x \, \in \, [0, \, 1]$$

where C_d is the drag coefficient, x is the x–coordinate of a point on the aerofoil, y is the y–coordinate of a point on the optimised aerofoil, and $y_{baseline}$ is the y–coordinate of the corresponding point on the initial aerofoil.

As opposed to the aerofoil used by Vassberg $et\ al.$,[4] a modified NACA 0012 aerofoil with zero–thickness trailing edge is defined as

$$y = \pm 0.6 \left(0.2969 \sqrt{x} \, - \, 0.1260 \, x \, - \, 0.3516 \, x^2 \, + \, 0.2843 \, x^3 \, - \, 0.1036 \, x^4 \right) \qquad (8)$$

where $x \in [0, \, 1]$. The zero–thickness trailing edge is achieved through a modification of the x^4 coefficient.

2.   Grid Convergence Study

Since the NACA 0012 aerofoil is symmetric and $\alpha \, = \, 0$ deg in this optimisation case, the corresponding flowfield is symmetric as well. Thus, only the upper surface of the aerofoil (i.e. half model) is taken for study unless otherwise specified, which saves computational cost by reducing the mesh size. A H–topology structured mesh is generated using the Pointwise software. The computational domain and mesh are shown in Figure 5. The farfield boundary has a semicircle shape and is located at a distance of 50 chord lengths away from the aerofoil. The aerofoil and farfield are connected by symmetry boundaries. The coarse mesh has a size of 129×65, where 129 grid points are distributed on the upper aerofoil surface. Small grid spacing is set at both the leading edge and the trailing edge in order to ensure that the aerofoil geometry is accurately represented and important flow features are captured. Based on the coarse mesh, the refined meshes are obtained by doubling the number of points in both chord–wise and normal directions. To establish grid convergence, four levels of mesh are considered, and the key mesh parameters are summarised in Table 1.

Table 1.   Case 1: mesh parameters for the NACA 0012 aerofoil grid convergence study.

Mesh Level	Mesh Size	Mesh Points	LE/TE Spacing
Coarse	129×65	$8,385$	$1.0 \cdot 10^{-3}$
Medium	257×129	$33,153$	$5.0 \cdot 10^{-4}$
Fine	513×257	$131,841$	$2.5 \cdot 10^{-4}$
Superfine	1025×513	$525,825$	$1.25 \cdot 10^{-4}$

The inviscid compressible flow analysis was then performed and the drag results for the baseline aerofoil are listed in Table 2. Note the C_d values are for the complete aerofoil geometry. Between the fine and superfine level of mesh, the resolution of 0.14 drag counts (1 drag count is equal to a C_d of $1 \cdot 10^{-4}$) is achieved. It is also noticed that the coarse mesh can produce drag result with sufficient level of accuracy. Thus, the coarse level of mesh is taken for optimisation unless otherwise stated.
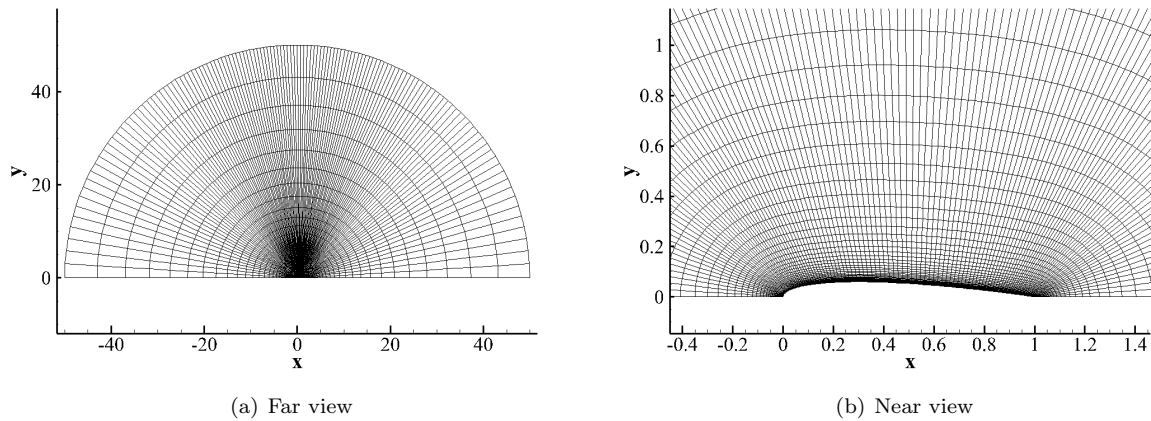
American Institute of Aeronautics and Astronautics

(a) Far view

(b) Near view

Figure 5. Case 1: computational domain and coarse mesh (129×65) **for the NACA 0012 aerofoil.**

Table 2. Case 1: drag results for the NACA 0012 aerofoil grid convergence study ($M = 0.85$, $\alpha = 0$ **deg**).

Mesh Level	C_d (Counts)
Coarse	468.02
Medium	469.00
Fine	469.30
Superfine	469.44

3. Optimisation Results

(a) Impact of Numerical Settings on Geometry Parameterisation

Both the Hicks–Henne bump functions and FFD are employed as the parameterisation method for the NACA 0012 aerofoil optimisation case. For each parameterisation method, several parameters need to be determined prior to the optimisation, and different settings of these parameters may generate different optimisation results. Thus, the influence of parameter settings on the optimisation performance is firstly investigated, with the purpose of finding a suite of settings that can produce the best optimisation results.

For Hicks–Henne bump functions, the bump amplitude coefficients a_i are defined as design variables and are set to have positive values, which transforms the constrained optimisation problem to an unconstrained one by satisfying the thickness constraint implicitly. In terms of bump maximum positions h_i, the optimisation was performed using two distribution approaches and the final drag results are plotted in Figure 6(a). It is apparent that the "one–minus–cosine" distribution approach outperforms the even distribution method by producing significantly lower drag counts. The only exception occurs in one case where the number of design variables is too small ($n_{dv} = 5$) and thus not representative. As it will be seen later, the shape deformations are mainly concentrated in the fore and aft sections of the aerofoil. Hence, the design space can be covered more accurately by distributing the bump functions using Eq. (4), and the "one–minus–cosine" distribution approach is used hereafter for the NACA 0012 aerofoil optimisation case.
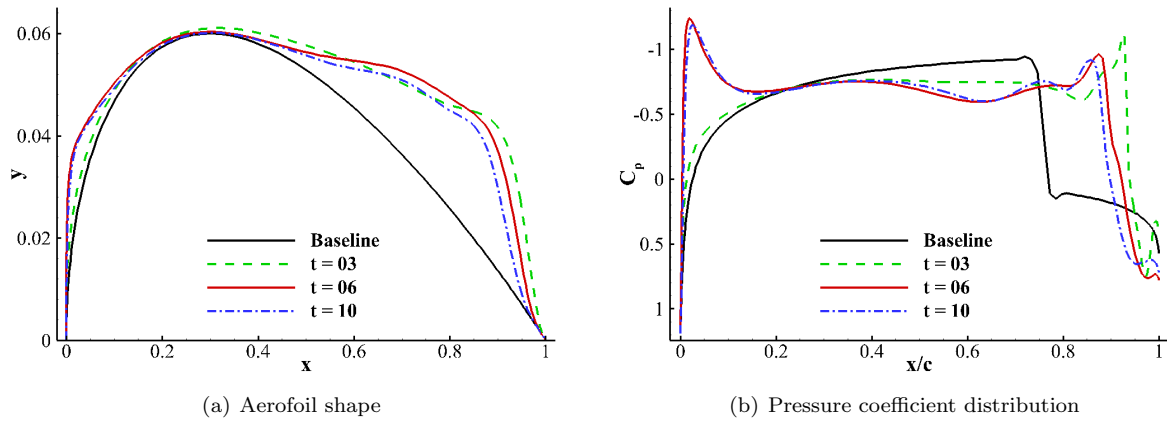
With regard to the bump width control parameter, a series of t values ranging from 1 to 15 are set for optimisation and the final drag results for $n_{dv} = 20$ and $n_{dv} = 30$ are plotted in Figure 6(b). It is clearly observed that there exists a sharp drop of C_d when t is increased from 3 to 5, and the results of $t = 3$ and $t = 6$ correspond to the two ends of the spectrum for optimisation performance. To find out the explanation for this fact, three representative groups of optimisation results with respect to $n_{dv} = 30$ are shown in Figure 7 for comparison. Concerning the optimised aerofoil shape, a primary difference is observed in the leading edge area. For $t = 6$ and $t = 10$, a significantly blunt leading edge is generated, which differs significantly from that obtained for $t = 3$. As mentioned earlier, more local shape control can be achieved with a relatively larger value of t. Specifically, setting $t = 6$ and $t = 10$ allows deforming the aerofoil in a narrow region near the leading edge. This, in turn, generates a suction peak for two larger values of t,

American Institute of Aeronautics and Astronautics

(a) Distribution function ($t = 8$)   (b) Bump width control parameter
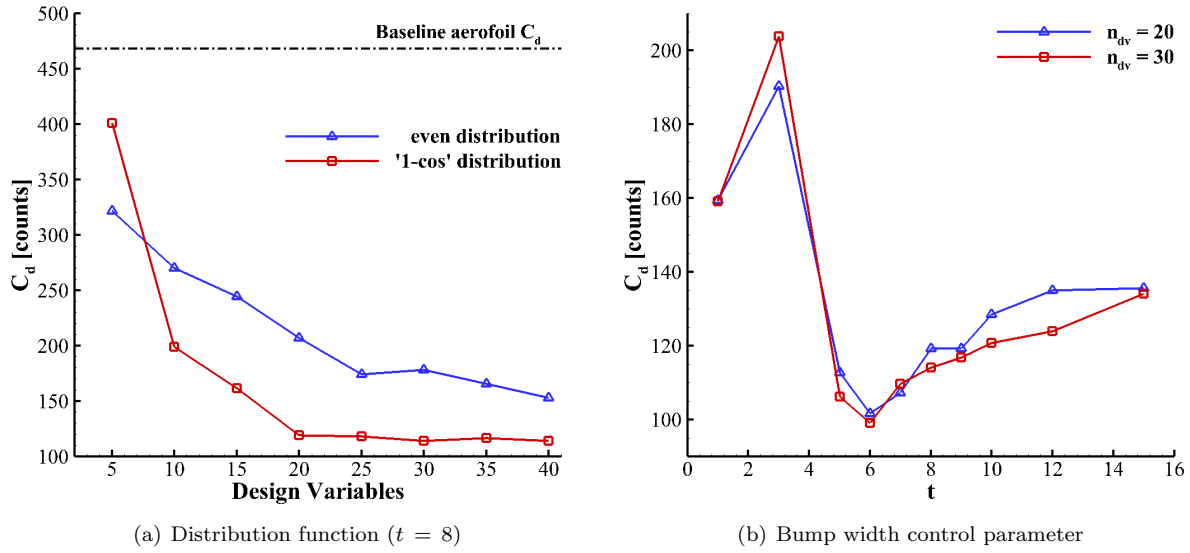
Figure 6. Case 1: influence of Hicks–Henne bump function parameters on drag coefficient ($M = 0.85$, $\alpha = 0$ deg).

whereas the case $t = 3$ generates a C_p distribution which is nearly unchanged from the baseline aerofoil near the leading edge. Due to the existence of pressure recovery after the suction peak, the two cases with larger values of t exhibit a weaker shock near the trailing edge and thus produce a lower wave drag. Since the wave drag contributes most to the total drag in this optimisation problem, it is not unexpected that the two larger values of t result in much better optimisation performance than $t = 3$. Based on Figure 6(b), $t = 6$ gives the lowest drag coefficient, and this setting of bump width control parameter is used hereafter for the NACA 0012 aerofoil optimisation case.

(a) Aerofoil shape   (b) Pressure coefficient distribution

Figure 7. Case 1: influence of Hicks–Henne bump width control parameter on optimisation results ($M = 0.85$, $\alpha = 0$ deg).

An example of the commonly–used FFD control point parameterisation is demonstrated in Figure 8(a), where the control points on the upper surface of FFD box are set as design variables. Owing to the symmetry characteristic of this optimisation problem, the FFD thickness approach embedded in SU2 framework is also employed in this work, which is illustrated in Figure 8(b). The thickness at specific chord–wise position of the aerofoil can be changed by manipulating a pair of control points, which are moved with the same amplitude but in opposite directions. Note the complete aerofoil geometry and corresponding mesh are generated for the FFD thickness approach. Regarding both FFD methods, the thickness constraint is again

American Institute of Aeronautics and Astronautics

satisfied implicitly by allowing the control points to move only in the outward direction as shown in Figure 8.

(a) FFD control point method

(b) FFD thickness method
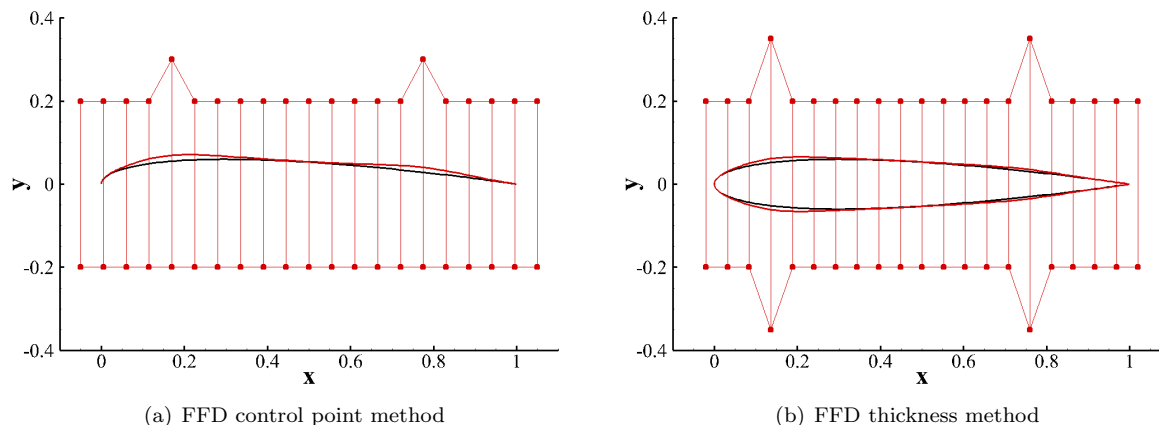
Figure 8.   Case 1: two FFD parameterisation approaches for the NACA 0012 aerofoil optimisation case. Baseline aerofoil is shown in black colour and deformed aerofoil in red.

The FFD box has a rectangular shape in this case and is defined by four boundaries. Technically speaking, optimisation can be successfully performed as long as these boundaries do not intersect with the embedded geometry and are located not too far from the aerofoil. Nonetheless, it is found in this study that the drag optimisation results have a dependence on different settings of the FFD box position. A combination of the four boundaries that can achieve the best optimisation performance are listed in Table 3, and these FFD box settings are used hereafter for the NACA 0012 aerofoil optimisation case.

Table 3.   Case 1: settings of FFD box position for the NACA 0012 aerofoil optimisation case.

	B_{upper}	B_{lower}	B_{left}	B_{right}
FFD control point method	0.2000	-0.2000	-0.0010	1.0010
FFD thickness method	0.0601	-0.0601	-0.0001	1.0001

(b) Dimensionality Study

To investigate the effect of design variable dimensionality, the optimisation was performed with the number of design variables ranging from 5 to 40. The three parameterisation methods introduced above have been employed. Figure 9 plots the final optimised aerofoil geometries and C_p distributions using Hicks–Henne bump function approach. With more design variables, the leading edge becomes blunter and the aft section of the aerofoil gets thicker, which indicates that a flatter aerofoil surface is created. Correspondingly, a suction peak is formulated in C_p distribution and becomes steeper as n_{dv} increases. The shock moves further downstream towards the trailing edge. Figure 10 displays the final deformed FFD boxes and aerofoil shapes using FFD thickness parameterisation method. As more control points are placed on the surface of FFD box, the optimiser is provided with more freedom to explore the design space. The convergence histories of the objective function are plotted in Figure 11. When increasing the number of design variables, more design cycles are needed for the optimiser to search the local minimum. In terms of the convergence performance of optimisation, Hicks–Henne bump function approach is superior than the other two parameterisation methods as it requires much less design iterations to meet the KKT condition (the tolerance is set as $1 \cdot 10^{-8}$ for this optimisation problem), especially for the cases with more design variables.

The final drag results of the dimensionality study are plotted in Figure 12. For both FFD control point and FFD thickness method, the drag coefficient monotonically decreases with more design variables, whereas for Hicks–Henne bump function approach, 15 design variables are sufficient to cover the design space. This fact is possibly caused by the difference of design variable distribution method. The bump functions are distributed using "one–minus–cosine" function and are clustered in the area where the surface sensitivities are relatively large. By contrast, the control points can only be placed uniformly on the surface of FFD box, which means that more design variables are needed for the optimiser to fully explore the design space. In terms of optimisation performance, approximately 80% of drag reduction is achieved with the best result for
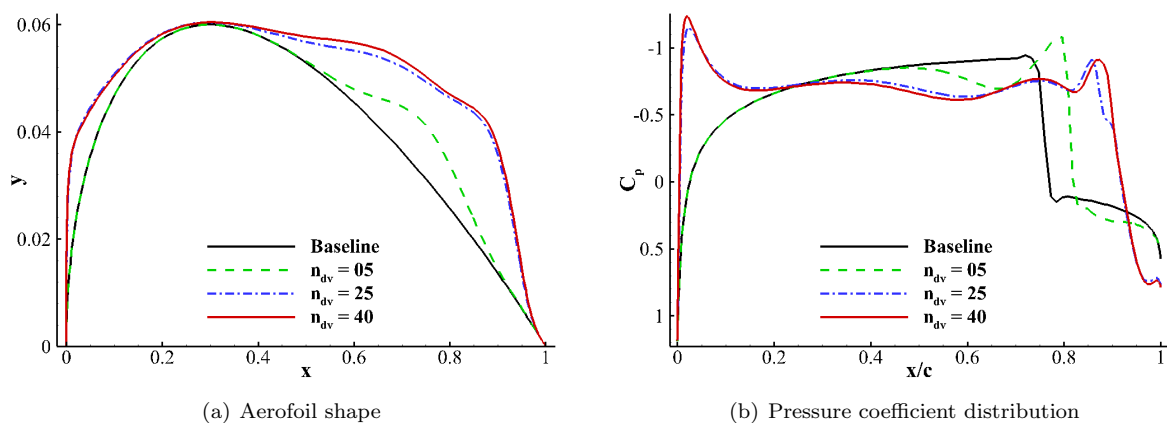
American Institute of Aeronautics and Astronautics

(a) Aerofoil shape

(b) Pressure coefficient distribution

Figure 9. Case 1: influence of design variable dimensionality on optimisation results using Hicks–Henne bump function approach ($M = 0.85$, $\alpha = 0$ deg).

(a) $n_{dv} = 10$

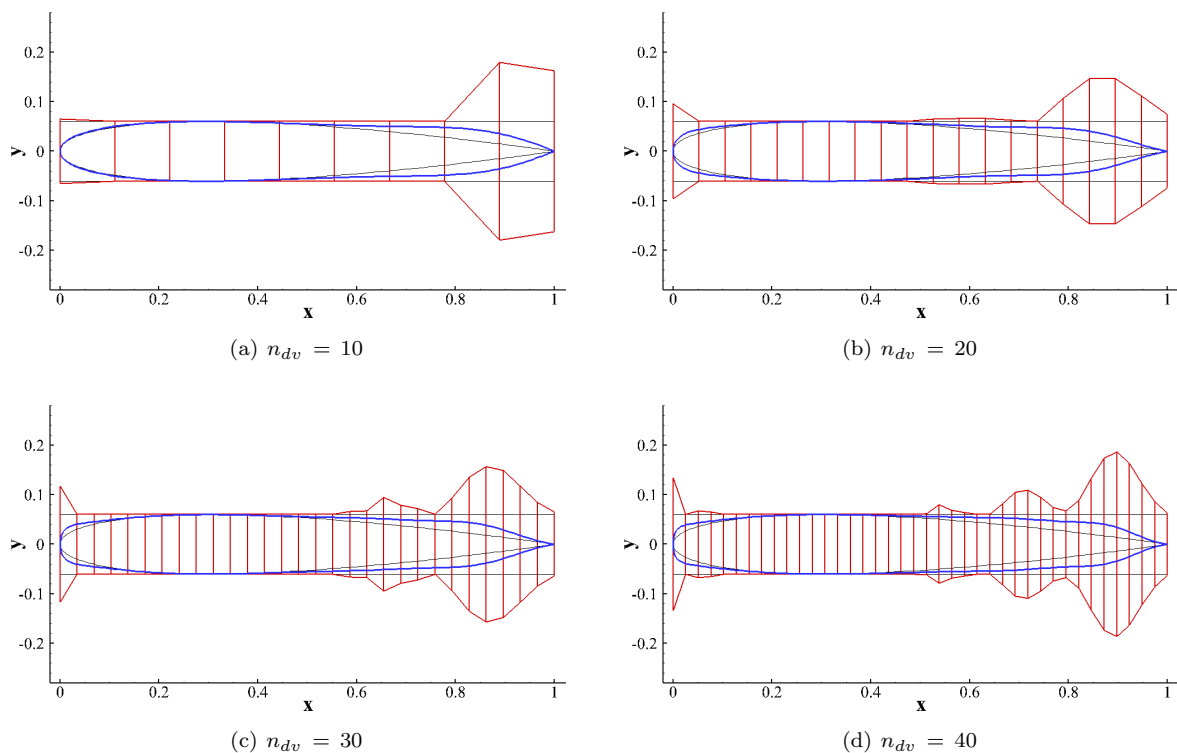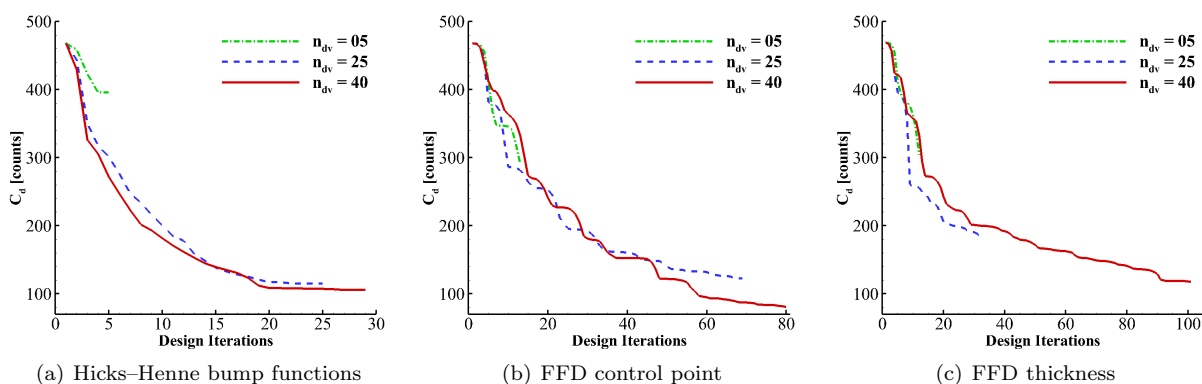(b) $n_{dv} = 20$

(c) $n_{dv} = 30$

(d) $n_{dv} = 40$

Figure 10. Case 1: FFD box deformation and geometry perturbation for dimensionality study using FFD thickness parameterisation method (original FFD box and aerofoil geometry in black, deformed FFD box in red and deformed aerofoil geometry in blue).

(a) Hicks–Henne bump functions   (b) FFD control point   (c) FFD thickness

Figure 11. Case 1: convergence histories for the NACA 0012 aerofoil optimisation using three parameterisation methods.

each parameterisation method. Specifically, for the case with 40 design variables, FFD control point method produces the lowest drag with 80.5 counts, which corresponds to 82.8% of drag reduction. The optimised aerofoil shapes and pressure distributions are then demonstrated and compared in Figure 13. Similarity is observed among the optimisation results, which implies that all of the three parameterisation methods are equally effective in this optimisation problem.
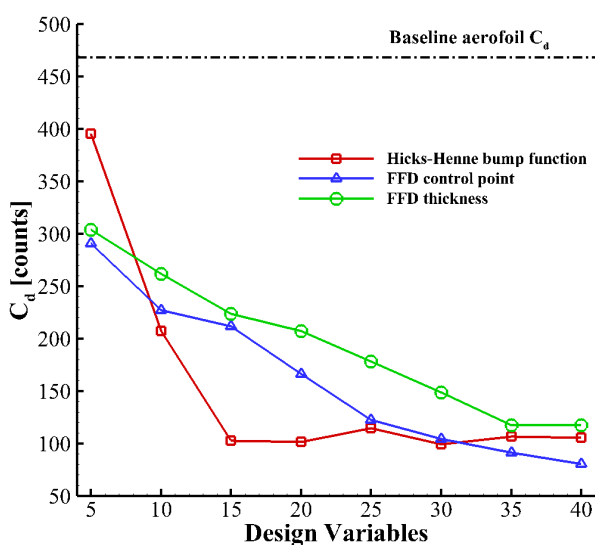
Figure 12. Case 1: drag coefficient results obtained from dimensionality study using three parameterisation methods ($M = 0.85$, $\alpha = 0$ deg).

(c) Results Analysis

Figure 14 displays the Mach contour for both the baseline and final optimised aerofoil using 30 Hicks–Henne bump functions. A rather flat surface is created by the optimiser through thickening the leading edge and aft section of the aerofoil. The strong shock is substantially weakened and is pushed further downstream, locating at around 90% chord–wise position. Then, a grid convergence study was performed on this optimised aerofoil and Table 4 lists the drag results. However, it is noticed that the drag value on the medium and two finer mesh levels is much higher than that on the coarse level. In order to find out the cause for this issue, the flow solutions obtained from the coarse and medium mesh are demonstrated in Figure 15 for comparison. It is obvious that a single shock is observed on the coarse mesh and a double shock on the medium mesh, which indicates that non–unique solutions may exist on such an aerofoil geometry at the design point. Note that the same phenomenon is also found on the optimised aerofoil obtained from optimisation using FFD parameterisation approaches and hence not repeated here. Besides, the presence of non–unique numerical

(a) Aerofoil shape

(b) Pressure coefficient distribution
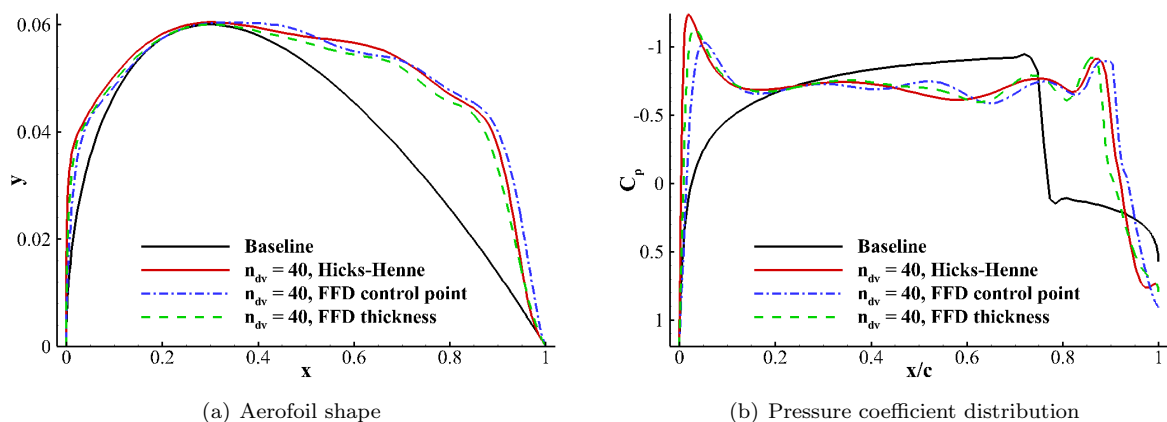
Figure 13. Case 1: comparison of optimisation results obtained from using three parameterisation methods ($M = 0.85$, $\alpha = 0$ deg, and $n_{dv} = 40$).

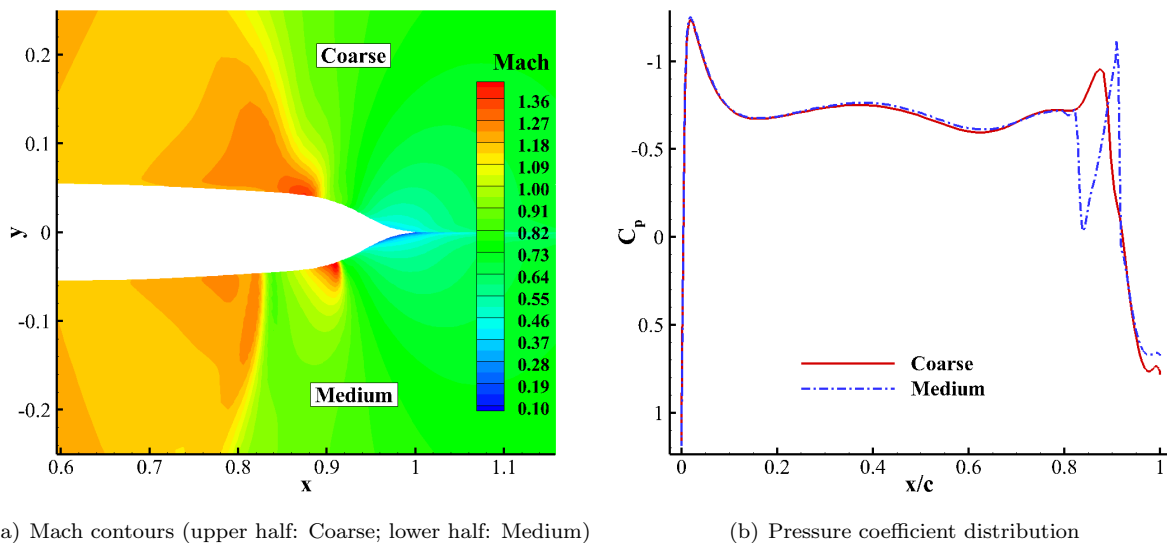solutions for this ADODG optimisation case is also noticed by other researchers.[3, 10, 11]

(a) Baseline aerofoil

(b) Optimised aerofoil
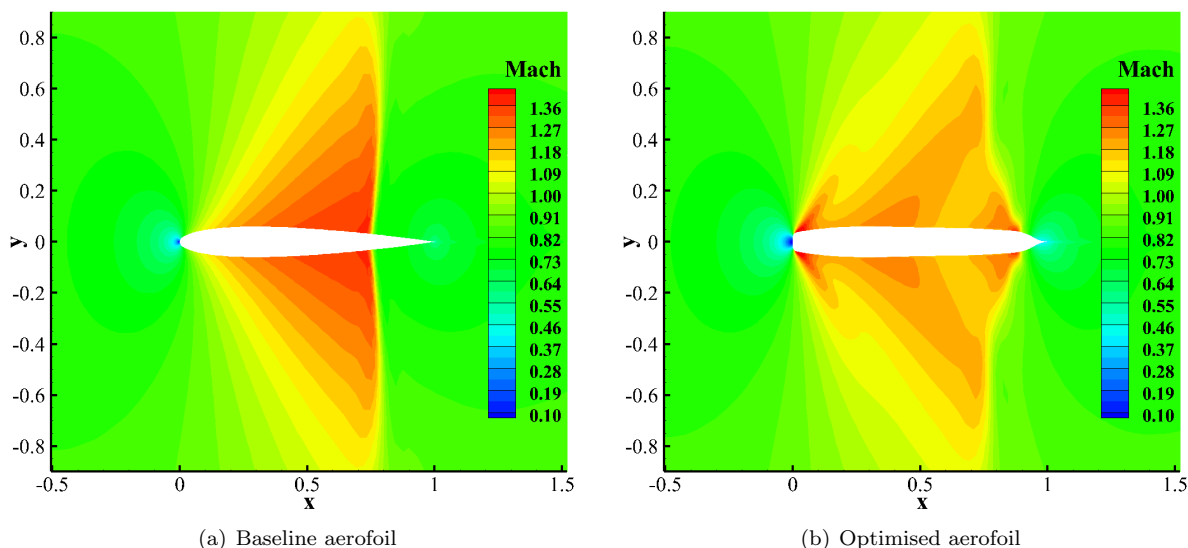
Figure 14. Case 1: Mach contours for baseline and optimised NACA 0012 aerofoil using Hicks–Henne bump function parameterisation method ($M = 0.85$, $\alpha = 0$ deg, and $n_{dv} = 30$).

To further investigate the issue of non–uniqueness, the inviscid flow analysis was conducted on both the coarse and medium mesh for the optimised aerofoil, which is obtained from optimisation with 30 design variables using Hicks–Henne bump function parameterisation approach. The Mach number was swept up and down in a small range around the design point ($M = 0.85$), and each flow simulation was initialised using the converged solution from the previous step. The results are then illustrated in Figure 16. Hysteresis behaviour is observed for the drag coefficient within a narrow Mach band and shows mesh dependence. For the optimised aerofoil on coarse mesh, hysteresis does not exist at the design point, and instead occurs at a lower Mach number. Thus, a unique flow solution can be obtained at the design point, which is shown in the upper half part of Figure 15(a). On the other hand, for the optimised aerofoil on medium mesh, the design point falls into the drag bifurcation region. Hence, the flow analysis of a clean start at the design point corresponds to the solution obtained from Mach sweep in the upward direction, which has a double shock as shown in the lower part of Figure 15(a). The problem of non–unique solutions in transonic flow for similar aerofoil geometries has been studied by Jameson *et al.*[23] and Ou *et al.*,[24] who found that non–unique

American Institute of Aeronautics and Astronautics

Table 4. Case 1: drag results of grid convergence study for the NACA 0012 optimised aerofoil ($M = 0.85$, $\alpha = 0$ deg, and $n_{dv} = 30$).

Mesh Level	C_d (Counts)
Coarse	99.14
Medium	142.34
Fine	141.58
Superfine	139.82

(a) Mach contours (upper half: Coarse; lower half: Medium)

(b) Pressure coefficient distribution

Figure 15. Case 1: comparison of flow solutions for the optimised aerofoil on coarse and medium level of mesh ($M = 0.85$, $\alpha = 0$ deg, and $n_{dv} = 30$).

American Institute of Aeronautics and Astronautics

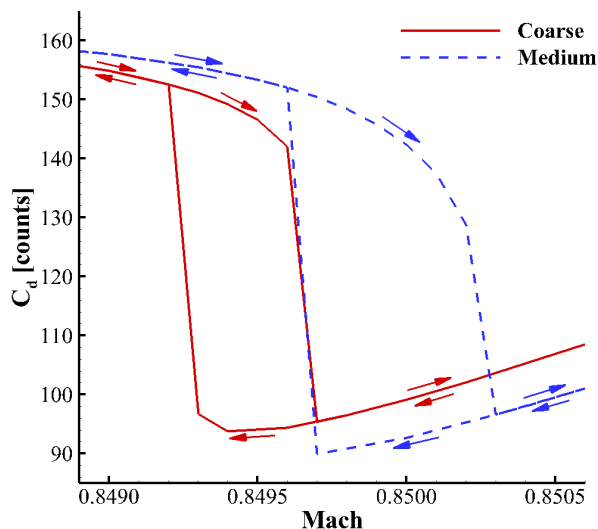solutions not only exist for steady Euler flows but also for unsteady RANS flows.

Figure 16. Case 1: flow analysis results showing hysteresis near the design point for the NACA 0012 optimised aerofoil ($\alpha = 0$ deg and $n_{dv} = 30$). Arrows indicate the sweep direction.

4. Case Summary

The NACA 0012 aerofoil optimisation case has been studied using three parameterisation approaches, which are Hicks–Henne bump functions, FFD control point method and FFD thickness method. Several conclusions are drawn by this exercise and summarised as follows:

- The optimised aerofoil exhibits a blunter leading edge and a thicker aft section compared with the baseline geometry. The strong shock at around three quarter–chord position is substantially weakened and pushed further downstream toward the trailing edge.

- The optimisation performance shows sensitivity to several parameters in Hicks–Henne and FFD parameterisation methods, such as bump function distribution, bump width control parameter and FFD box position. For this optimisation problem, the "one–minus–cosine" distribution for bump functions outperforms the even distribution approach, and the setting of $t = 6$ produces the lowest drag results.

- The impact of design variable dimensionality is investigated. It is found that 15 Hicks–Henne bump functions are sufficient to cover the design space, whereas more design variables are needed for FFD approaches. Around 80% of drag reduction is achieved for each parameterisation method, and Hicks–Henne bump function outperforms FFD approaches in terms of optimisation convergence speed.

- Non–unique flow solutions occur within a narrow Mach number spectrum around the design point, and the hysteresis loop shows dependence on mesh resolution. The optimised aerofoil with nearly flat surface is ill posed in inviscid transonic flow.

B. Case 2: Drag Minimisation of the RAE 2822 Aerofoil in Transonic Viscous Flow

1. Problem Description

The second optimisation problem studied is the drag minimisation of the RAE 2822 aerofoil in viscous, transonic flow. The freestream Mach number is 0.734, and the Reynolds number is $6.5 \cdot 10^6$. The lift coefficient is constrained to 0.824, the pitching moment coefficient (evaluated at the quarter–chord) must be no less than -0.092, and the aerofoil area must be greater than or equal to the initial aerofoil area during

American Institute of Aeronautics and Astronautics

the optimisation process. The optimisation problem is written as

$$
\begin{aligned}
\text{Minimise:} \quad & C_d \\
\text{Subject to:} \quad & C_l = 0.824 \\
& C_m \geq -0.092 \\
& S \geq S_0
\end{aligned}
$$

where C_d, C_l and C_m are the drag, lift, and pitching moment coefficients, respectively, and S and S_0 are the optimised and initial aerofoil areas, respectively. The coordinates of the RAE 2822 aerofoil are obtained from the UIUC Aerofoil Coordinates Database[b].

2. Grid Convergence Study

A C–topology structured mesh is generated for the RAE 2822 optimisation case. The computational domain is bounded by a no–slip aerofoil surface and a farfield located at a distance of 20 chord lengths from the aerofoil. Figure 17 illustrates the coarse mesh that has size 385×65, where 257 grid points are distributed on the aerofoil surface and 65 grid points downstream the trailing edge in the x direction. Small grid spacing is set at both the leading and trailing edges of the aerofoil. The off–wall spacing is also set to ensure that the y^+ value is below 1.0 on the aerofoil. To establish grid convergence, four levels of mesh are generated with the same topology. Based on the coarse mesh, the refined meshes are produced through multiplying the number of points on each edge by a factor of $\sqrt{2}$. The key parameters for those meshes are summarised in Table 5.
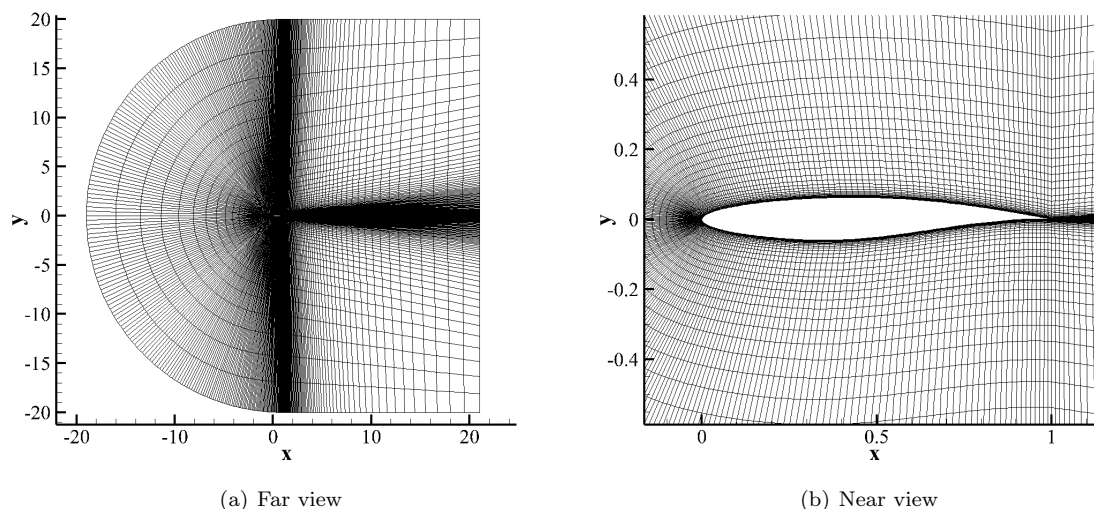

| (a) Far view | (b) Near view |

Figure 17. Case 2: computational domain and coarse mesh (385×65) for the RAE 2822 aerofoil.

Table 5. Case 2: mesh parameters for the RAE 2822 aerofoil grid convergence study.

Mesh Level	Mesh Size	Mesh Points	LE Spacing	TE Spacing	Off–wall Spacing
Coarse	385×65	24,960	$2.0 \cdot 10^{-4}$	$1.0 \cdot 10^{-2}$	$1.0 \cdot 10^{-5}$
Medium	549×93	50,964	$1.4 \cdot 10^{-4}$	$7.1 \cdot 10^{-3}$	$7.1 \cdot 10^{-6}$
Fine	769×129	99,072	$1.0 \cdot 10^{-4}$	$5.0 \cdot 10^{-3}$	$5.0 \cdot 10^{-6}$
Superfine	1097×185	202,760	$7.1 \cdot 10^{-5}$	$3.5 \cdot 10^{-3}$	$3.5 \cdot 10^{-6}$

The compressible RANS simulation was then conducted on each grid level. Note that the angle of attack was iteratively updated during the flow analysis to meet the target lift coefficient. The flow results of the

---

[b]http://m-selig.ae.illinois.edu/ads/coord_database.html

American Institute of Aeronautics and Astronautics

baseline aerofoil are listed in Table 6. Besides, the initial aerofoil area is evaluated to be 0.077867. For the purpose of saving computational cost, the coarse mesh is chosen for optimisation in this work.

Table 6. Case 2: results for the RAE 2822 aerofoil grid convergence study at $M = 0.734$ and $R_e = 6.5 \cdot 10^6$.

Mesh Level	C_l	C_d (Counts)	C_m	α [deg]
Coarse	0.82400	241.24	-0.089	3.1848
Medium	0.82400	236.35	-0.091	3.1071
Fine	0.82400	232.27	-0.092	3.0654
Superfine	0.82400	228.81	-0.093	3.0450

3. Optimisation Results

(a) Impact of Numerical Settings on Geometry Parameterisation

For the RAE 2822 aerofoil, Hicks–Henne bump functions and FFD control point approach are employed as the parameterisation method. In order to satisfy the lift constraint, the angle of attack is set as design variable in this optimisation problem. Regarding these two parameterisation methods, the impact of parameter settings on optimisation performance is firstly investigated. Both even and "one–minus–cosine" distribution approach are used for bump maximum positions h_i. Four settings of bump width control parameter t (ranging from 1 to 10) are specified for this case. The final drag results are plotted in Figure 18(a) and 18(b). It is apparent that the same level of optimisation performance is achieved using different parameter settings, which implies that this optimisation case is insensitive to either bump function distribution or bump width control parameter. As such, the even distribution is selected and the setting of $t = 3$ is used in this work hereafter. With respect to FFD parameterisation, the optimisation performance also shows independence of FFD box positions, the results of which are thus not provided herein.


(a) Bump function distribution $(t = 3)$ (b) Bump width control parameter   (c) Dimensionality
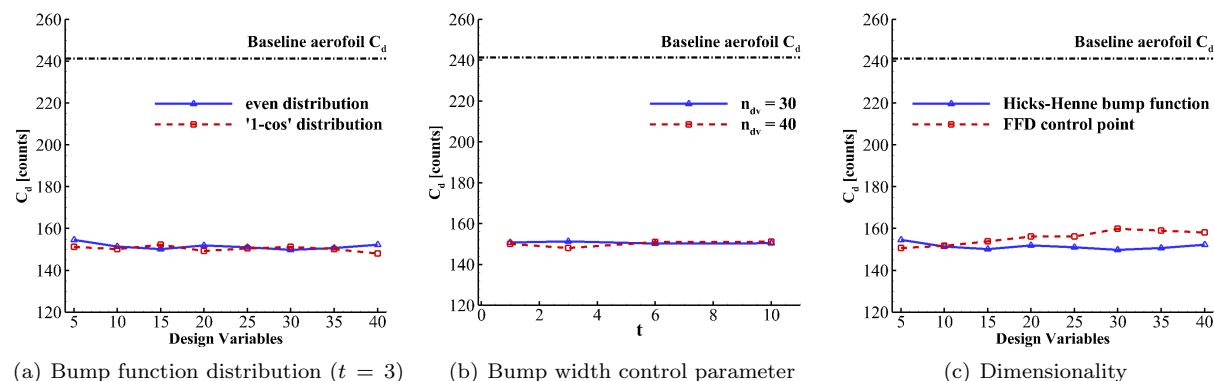
Figure 18. Case 2: influence of Hicks–Henne bump function parameters and design variable dimensionality on drag coefficient ($M = 0.734$, $C_l = 0.824$, and $R_e = 6.5 \cdot 10^6$).

(b) Dimensionality Study

The effect of design variable dimensionality was then investigated and the final drag results are demonstrated in Figure 18(c). It is observed that the optimisation performance does not improve with more design variables, and as few as 5 design variables are sufficient to cover the design space. Figure 19 plots the optimisation results obtained from using Hicks–Henne parameterisation method, and similar behaviour is found between $n_{dv} = 5$ and $n_{dv} = 40$. On the upper surface of the aerofoil, the curvature in the fore section is reduced, which alleviates the flow acceleration and hence eliminates the shock; whereas on the lower surface, the increase of curvature is primarily to satisfy the area constraint. It is also noticed from Figure 18(c) that both parameterisation methods are equally effective for this optimisation problem, achieving approximately 38% of drag reduction. For the case with 5 design variables, Figure 20 compares the optimisation results obtained from using Hicks–Henne and FFD approach. Similar pattern exists for the

American Institute of Aeronautics and Astronautics

surface perturbation as well as C_p distribution. The pressure discontinuity is replaced by a smooth pressure recovery, thus eliminating the shock wave.

(a) Aerofoil shape   (b) Pressure coefficient distribution
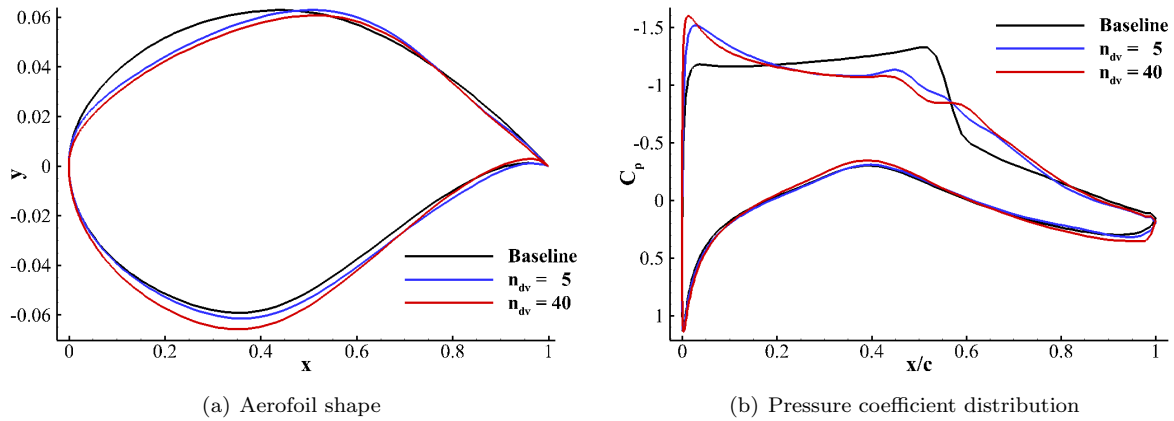
Figure 19. Case 2: influence of design variable dimensionality on optimisation results using Hicks–Henne bump function approach ($M = 0.734$, $C_l = 0.824$, and $R_e = 6.5 \cdot 10^6$).

(a) Aerofoil shape   (b) Pressure coefficient distribution
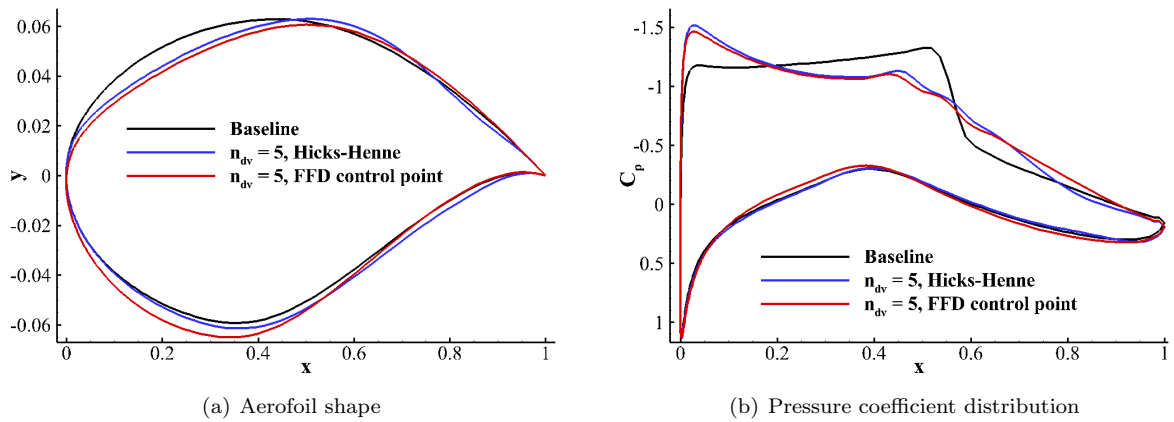
Figure 20. Case 2: comparison of optimisation results obtained from using two parameterisation methods ($M = 0.734$, $C_l = 0.824$, $R_e = 6.5 \cdot 10^6$, and $n_{dv} = 5$).

The convergence histories for the objective function are displayed in Figure 21. For Hicks–Henne bump function approach, substantial drag reduction is achieved within a few design cycles since that the optimiser could easily find the local optimum in the design space. For FFD control point approach, however, an issue of convergence difficulty occurs, and more design iterations are required to meet the KKT condition, of which the tolerance is set as $1 \cdot 10^{-6}$ for this optimisation case. To find out the cause behind this issue, the drag convergence history versus function evaluations is illustrated in Figure 22 for the case with 30 FFD design variables. After monotonic reduction in early designs, the drag coefficient exhibits oscillations in later optimisation process, generating spike values with dramatic drag increase. The optimisation results obtained from two consecutive function evaluations are compared in Figure 23. While the aerofoil geometries are nearly identical, the pressure distributions, however, show different patterns. The Mach contours are then compared in Figure 24. The primary distinction is that one case exhibits single pressure recovery feature and the other produces double pressure recovery, which indicates non-unique flow solutions on the optimised aerofoil. The existence of non–unique solutions would lead to non–smooth design space and thus cause difficulty for the gradient–based optimiser to search the local minimum, which explains the poor convergence performance for some of the optimisations.

Similar to the NACA 0012 case, a series of RANS flow analyses were run for the RAE 2822 optimised aerofoil, which is obtained from optimisation using 30 FFD design variables. The angle of attack was swept
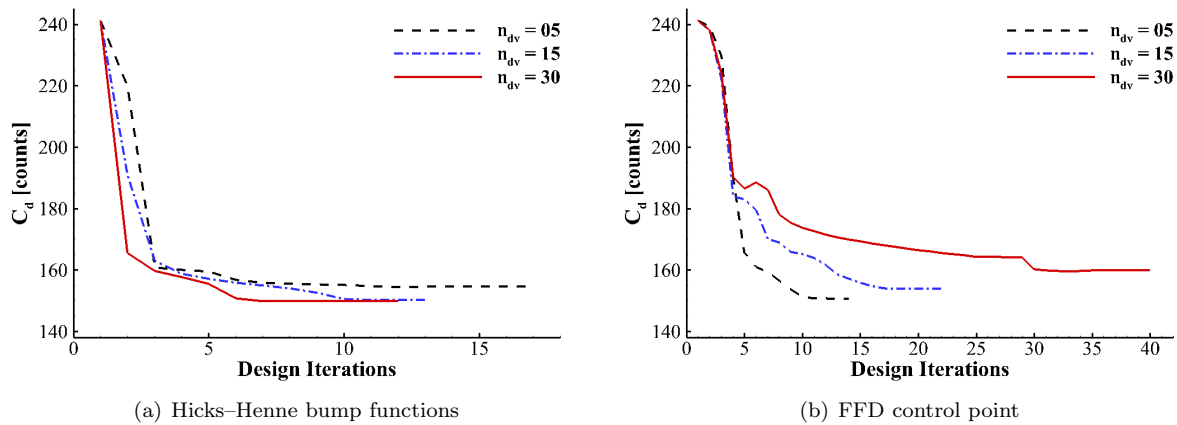
(a) Hicks–Henne bump functions

(b) FFD control point

Figure 21. Case 2: convergence histories for the RAE 2822 aerofoil optimisation using two parameterisation methods.
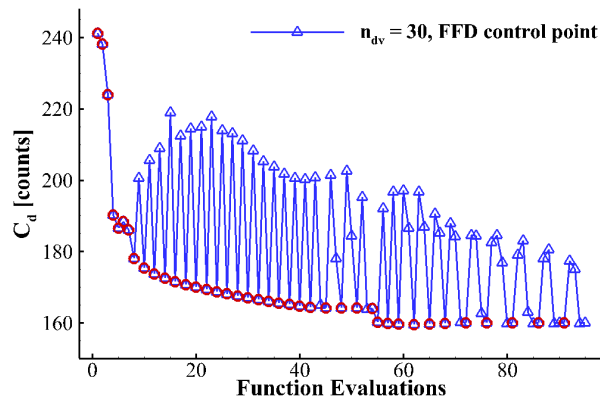

Figure 22. Case 2: convergence history of the RAE 2822 optimisation with 30 design variables using FFD parameterisation method (red circles represent gradient evaluations or design iterations).
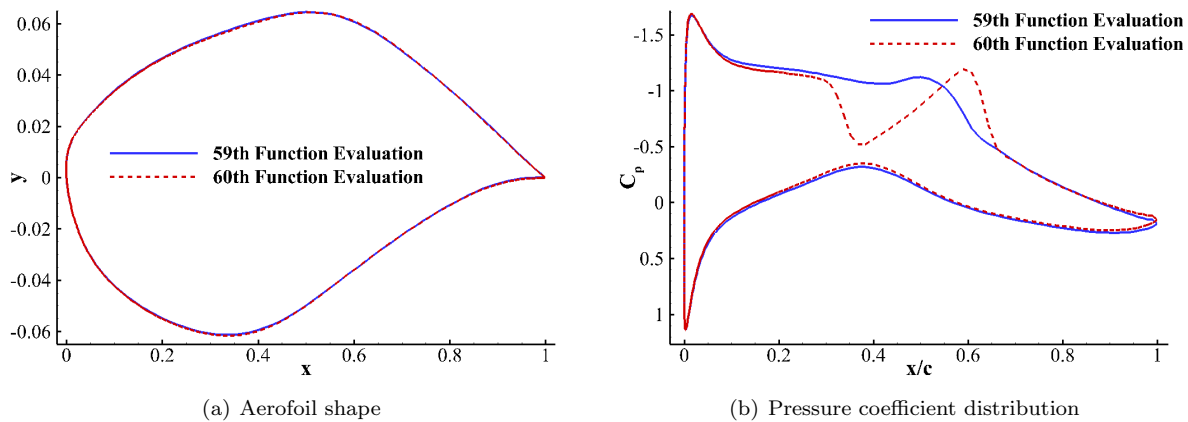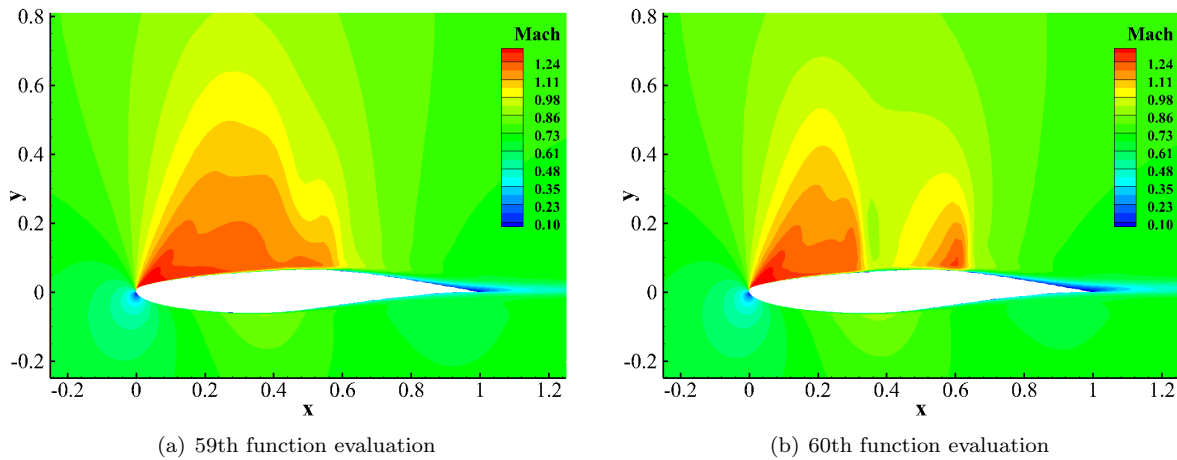

(a) Aerofoil shape

(b) Pressure coefficient distribution

Figure 23. Case 2: comparison of results obtained from two consecutive (59th and 60th) function evaluations in RAE 2822 optimisation using FFD parameterisation method ($M = 0.734$, $C_l = 0.824$, $R_e = 6.5 \cdot 10^6$, and $n_{dv} = 30$).

American Institute of Aeronautics and Astronautics

(a) 59th function evaluation

(b) 60th function evaluation

Figure 24. Case 2: comparison of Mach contours for non–unique flow solutions in RAE 2822 optimisation using FFD parameterisation method ($M = 0.734$, $C_l = 0.824$, $R_e = 6.5 \cdot 10^6$, and $n_{dv} = 30$).

up and down in a small range with an increment of 0.01 deg, and each flow simulation was restarted from the previous converged solution. The drag results are illustrated in Figure 25. It is found that hysteresis loop exist on the optimised aerofoil. As the design point, $\alpha = 3.1848$ deg, falls into the drag bifurcation region, two distinct flow solutions are thus obtained. The solution with single pressure recovery corresponds to the lower drag, and the solution with double pressure recovery generates a higher drag. It should be noted that the occurrence of non–unique solutions in the RAE 2822 aerofoil optimisation case was also observed by LeDoux *et al.*[11] and Lee *et al.*[3] Nonetheless, the cause for this problem has not been fully understood yet and requires further study, which is beyond the scope of this paper.
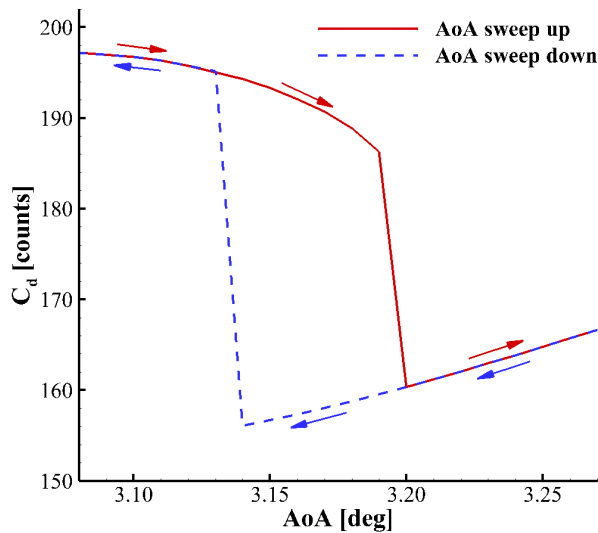

Figure 25. Case 2: flow analysis results showing hysteresis near the design point for the RAE 2822 optimised aerofoil ($M = 0.734$, $R_e = 6.5 \cdot 10^6$, and $n_{dv} = 30$). Arrows indicate the sweep direction.

(c) Results Analysis

Figure 26 displays the Mach contours for both the baseline and final optimised aerofoil using 20 Hicks–Henne bump functions. The strong shock on the upper surface is eliminated and the wave drag is thus removed. For this optimisation case, the convergence histories of constraints are plotted in Figure 27. Firstly, the lift coefficient initially deviates from the value of 0.824 because the major shape deformation is performed in the first few design steps. Then the lift coefficient gradually recovers to the target value and

American Institute of Aeronautics and Astronautics

finally satisfies the constraint. Secondly, for the pitching moment coefficient, despite an initial decrease, the optimisation seeks to provide designs with higher C_m values, which leaves more margin for this constraint. Thirdly, the area constraint is basically satisfied throughout the optimisation process, and the final design provides with an area of 0.077857, which violates the constraint by only 0.01%.

(a) Baseline aerofoil

(b) Optimised aerofoil
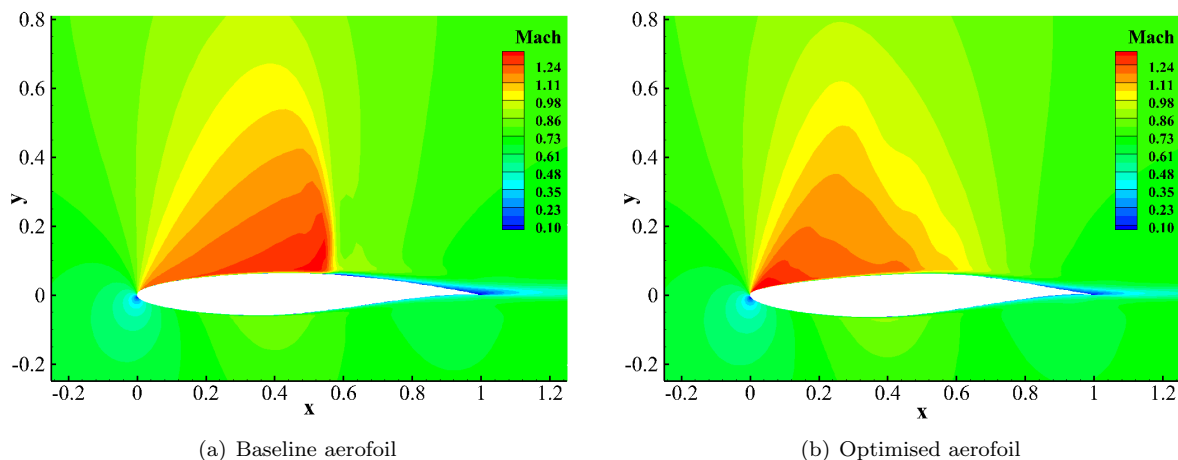
Figure 26. Case 2: Mach contours for baseline and optimised RAE 2822 aerofoil using Hicks–Henne parameterisation method ($M = 0.734$, $C_l = 0.824$, $R_e = 6.5 \cdot 10^6$, and $n_{dv} = 20$).

(a) Lift constraint

(b) Pitching moment constraint

(c) Area constraint
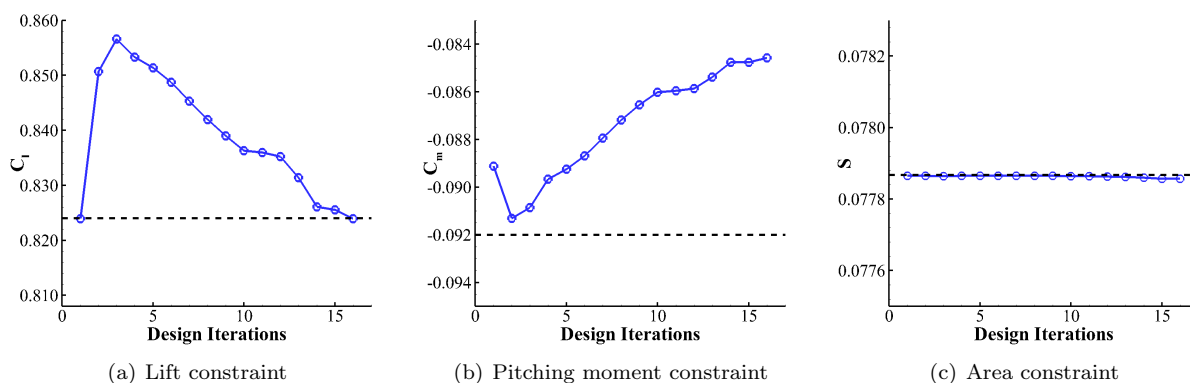
Figure 27. Case 2: convergence histories of constraints in the RAE 2822 optimisation using Hicks–Henne parameterisation method ($n_{dv} = 20$). Dashed line indicates the desired value for specific constraint.

A grid convergence study was performed for the optimised aerofoil and Table 7 lists the drag results on four grid levels. The drag resolution between fine and superfine mesh is 2.32 counts. The pressure distributions are then compared in Figure 28(a) and the Mach contour on superfine mesh is plotted in Figure 28(b). It is observed that stair–like pressure recovery feature exists on the medium and two finer meshes. Since the coarse mesh is used for optimisation in this case, it is thus expected that further drag reduction may be achieved if a finer level of mesh is used for optimisation.

4.   Case Summary

The RAE 2822 aerofoil optimisation has been performed using two parameterisation methods, which are Hicks–Henne bump functions and FFD control point approach. From the results presented for this case, several findings are summarised as follows:

- The aerofoil shape deformation primarily exists in the fore section. Compared to the baseline aerofoil, a relatively flat surface is created on the upper side to reduce flow acceleration and thus eliminate the shock, and the curvature on the lower surface is increased to maintain the area.

American Institute of Aeronautics and Astronautics

Table 7. Case 2: drag results of grid convergence study for the RAE 2822 optimised aerofoil ($M = 0.734$, $\alpha = 3.1850$ deg, $R_e = 6.5 \cdot 10^6$, and $n_{dv} = 20$).

Mesh Level	C_d (Counts)
Coarse	151.35
Medium	151.19
Fine	149.56
Superfine	147.24
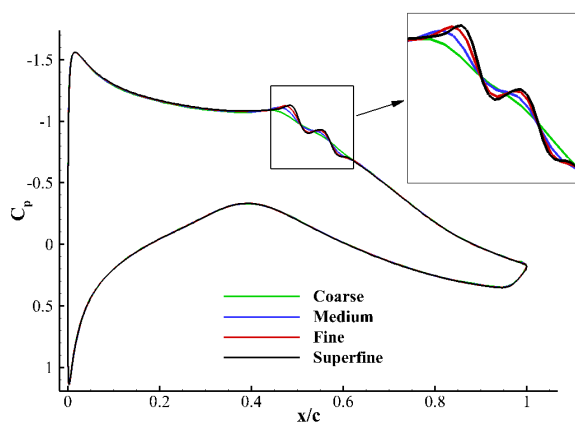
(a) Pressure coefficient distribution
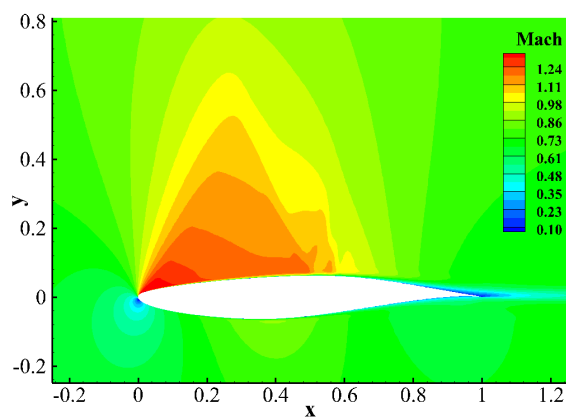
(b) Mach contour on superfine mesh (1097×185)

Figure 28. Case 2: grid convergence study for the RAE 2822 optimised aerofoil using Hicks–Henne parameterisation method ($M = 0.734$, $\alpha = 3.1850$ deg, $R_e = 6.5 \cdot 10^6$, and $n_{dv} = 20$).

American Institute of Aeronautics and Astronautics

- The optimisation performance is insensitive to the parameter settings in parameterisation methods, including bump function distribution, bump width control parameter and FFD box position. Approximately 38% of drag reduction is achieved using either of these two parameterisation methods.

- The effect of dimensionality on optimisation performance was investigated. It is found that a few design variables are sufficient to cover the design space, which indicates the design space can be easily explored in this case.

- Non–unique flow solutions are observed on the optimised aerofoil, and hysteresis behaviour is found to exist in a narrow range around the design point in angle of attack sweep analysis.

C.   Case 3: Twist Optimisation of the NACA 0012 Wing in Subsonic Inviscid Flow

1.   Problem Description

The third optimisation problem is the induced drag minimisation of a rectangular wing with NACA 0012 (defined by Eq. (8)) sections in inviscid, subsonic flow. The freestream Mach number is 0.5, and the target lift coefficient is 0.375. The design variables are the twist of sections along the span and about the trailing edge. The purpose of this case is to produce a lift distribution that is close to elliptical and a span efficiency factor approximately equal to one. This optimisation problem is written as

$$
\begin{aligned}
\text{Minimise:} \quad & C_D \\
\text{w.r.t:} \quad & \gamma\,(y) \\
\text{Subject to:} \quad & C_L \,=\, 0.375
\end{aligned}
$$

where C_D and C_L are the drag and lift coefficients of the wing, respectively, and $\gamma\,(y)$ is the twist distribution along the wing span.

2.   Geometry and Grid

The baseline geometry is a rectangular wing with NACA 0012 sections. The semi–span length is $3.06\,c$, where c is the chord length; the wing planform is rectangular over the first $3.0\,c$ and the last $0.06\,c$ is enclosed by a round wing–tip cap, which is a surface of revolution based on the NACA 0012 aerofoil. For the consideration of non–dimensionalisation, the reference semi–span area and semi–span length are defined as $S\,=\,3\,c^2$ and $b/2\,=\,3\,c$, respectively.
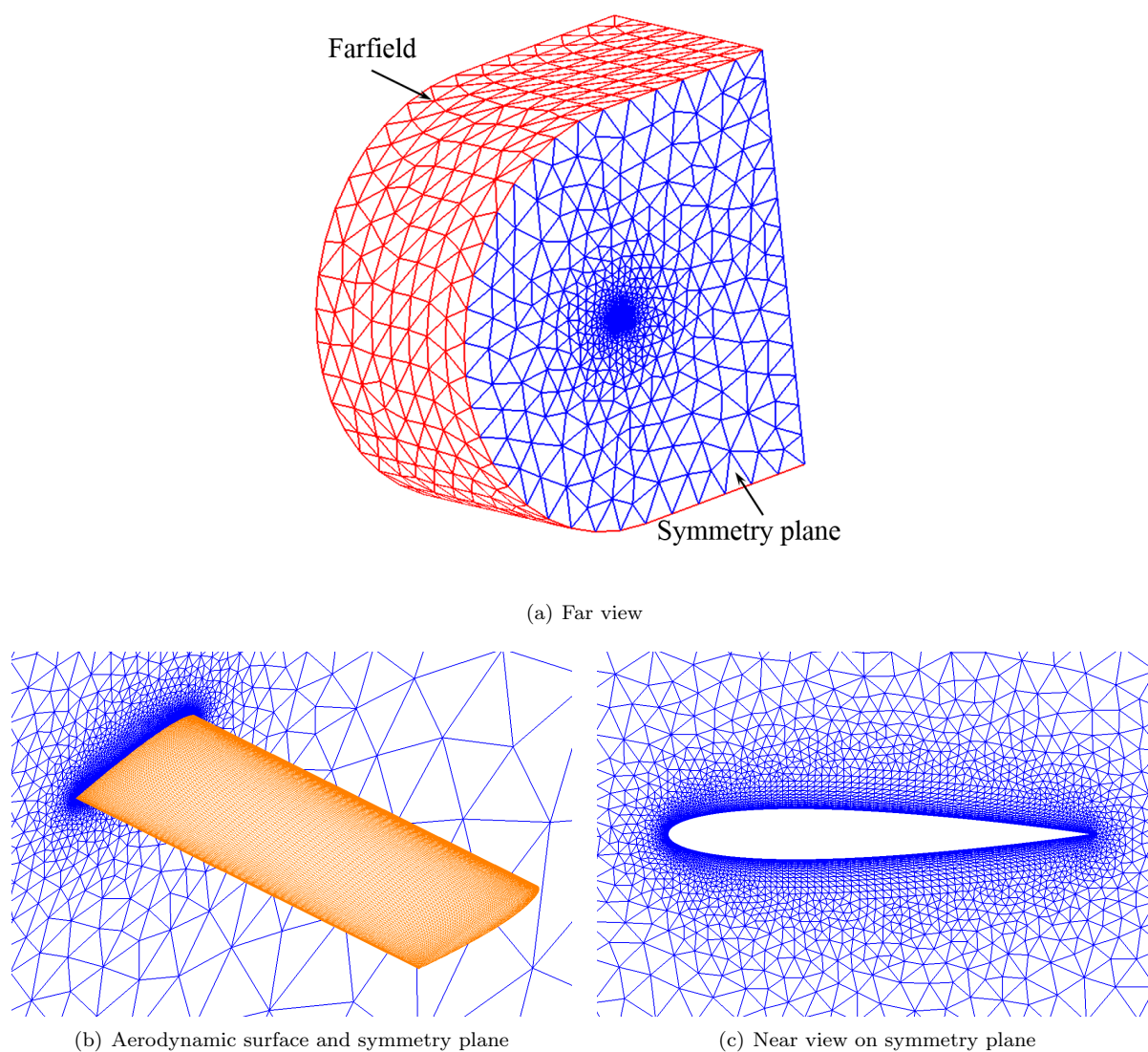
An unstructured mesh was generated using Pointwise. The computational mesh is displayed in Figure 29. The farfield is located at a distance of $20\,c$ away from the wing geometry. The grid points are clustered near the leading and trailing edge and also clustered at the wing tip to capture the flow features. The mesh consists of nearly 1.27 million cells and was found adequate to guarantee grid independent solutions. To obtain the desired $C_L\,=\,0.375$, the angle of attack was iteratively updated in the flow simulation and was determined to be $\alpha\,=\,4.2580$ deg.

3.   Optimisation Results

The FFD parameterisation approach is employed in the 3D optimisation problem. As shown earlier in Figure 4(a), the rectangular wing is enclosed by a FFD box. The control points are distributed uniformly on the surface of the FFD box. The design variables are specified as the twist of the FFD box at different span–wise stations, and the rotation at every span–wise station is centred about the trailing edge. In this work, the angle of attack is fixed, while the twist at the wing root is allowed to vary. A series of optimisations were performed with the number of design variables ranging from 3 to 11. The drag coefficient and the span efficiency factor are plotted in Figure 30. Approximately one drag count reduction is achieved for all cases and the variation of drag results is very trivial. Correspondingly, the optimised span efficiency e has improved with around one percent increase. As suggested in the Ref.,[1] a modified span efficiency factor e_0 is also used, which is defined as

$$
e_0 \,=\, \frac{C_L^2}{\pi\,\Lambda\,(C_D\,-\,C_{D_0})} \tag{9}
$$

where Λ and C_{D_0} are the wing aspect ratio and zero lift drag, respectively. It would provide a better estimate of the actual span efficiency by eliminating the spurious drag at $\alpha\,=\,0$ deg, which is attributed to

American Institute of Aeronautics and Astronautics

(a) Far view

(b) Aerodynamic surface and symmetry plane

(c) Near view on symmetry plane

Figure 29. Case 3: computational domain and mesh for the rectangular NACA 0012 wing.

American Institute of Aeronautics and Astronautics

the numerics of the flow solver. It is worth observing that the final optimised span efficiency e_0 is 0.967 in the best practice, which corresponds to an 1.26% improvement of the span efficiency factor.

(a) Drag coefficient

(b) Span efficiency factor
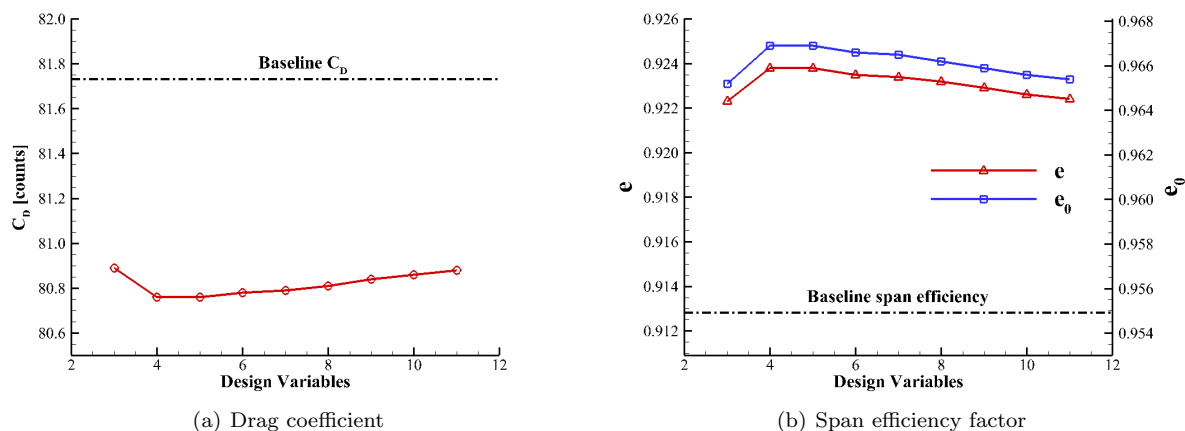
Figure 30. Case 3: drag coefficient and span efficiency factor evaluated on the optimised NACA 0012 wing with different number of design variables ($M = 0.5$, $\alpha = 4.2580$ deg).

Figure 31 plots the convergence histories of the objective function for three optimisation cases with different number of design variables. It is noticed that only a few design steps are required to yield the optimal solution. Since the $n_{dv} = 5$ case gives slightly better optimisation performance, the optimisation results are taken for analysis. Figure 32 displays the lift and twist distributions for the initial and optimised geometries. The initial load distribution has already shown an approximated elliptical pattern, and thus the optimiser can easily find the local minimum within several design iterations. The final load distribution shows good agreement with the theoretical elliptical distribution, which confirms the validity of the optimisation framework in this optimisation problem. The twist values reported in this study are measured relative to the angle of attack. As expected, the outboard sections produce negative twist to reduce the vortex drag, whereas the inboard sections generate positive twist to increase the sectional lift and hence maintain the required C_L. It should be noted that the lift coefficient constraint is satisfied during the optimisation process and thus not shown herein. Finally, the comparisons between original and deformed FFD boxes as well as wing geometries are illustrated in Figure 33. A small perturbation of the FFD box is observed, which leads to a smooth shape deformation on the wing surface geometry.
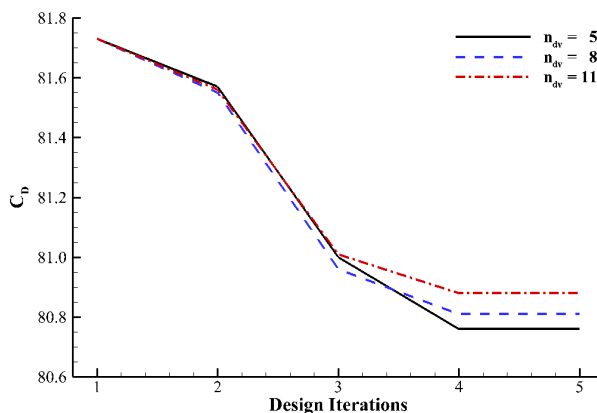
Figure 31. Case 3: convergence histories for the NACA 0012 wing twist optimisation.
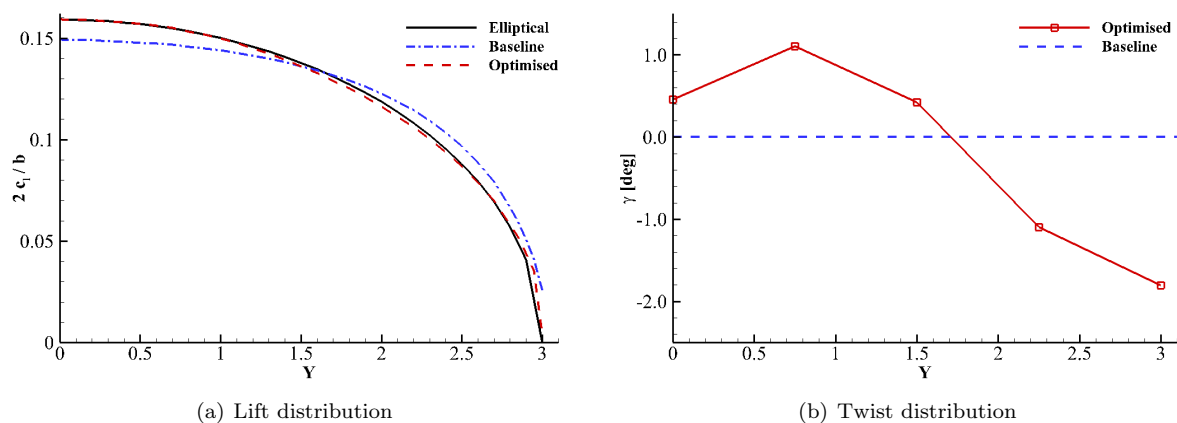
American Institute of Aeronautics and Astronautics

(a) Lift distribution

(b) Twist distribution

Figure 32. Case 3: lift and twist distributions for the initial and optimised wing geometries (M = 0.5, α = 4.2580 deg, and n_{dv} = 5); An elliptical lift distribution is also included for reference.
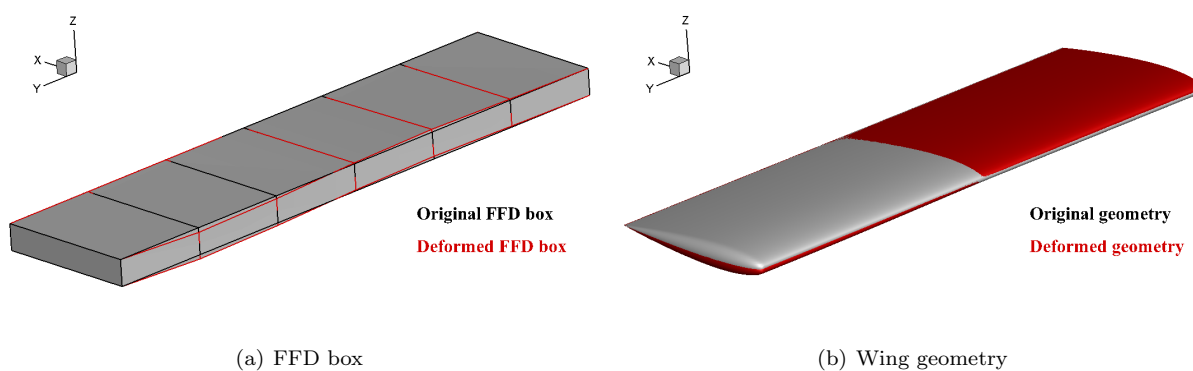

(a) FFD box

(b) Wing geometry

Figure 33. Case 3: original and deformed FFD boxes as well as wing geometries (n_{dv} = 5).

American Institute of Aeronautics and Astronautics

IV.   Conclusion

The open–source suite SU2 is employed to solve three benchmark optimisation problems defined by the AIAA ADODG. For the NACA 0012 aerofoil optimisation case, the optimised aerofoil shows a blunter leading edge and a thicker aft section compared with the baseline geometry. The strong shock is substantially weakened and pushed further downstream toward the trailing edge, reducing drag from 468.02 counts to 80.5 counts in the best practice. For the RAE 2822 aerofoil optimisation case, the curvature in the fore section of upper side is reduced to create a relatively flat surface. Correspondingly, the flow acceleration is eased and the shock wave is eliminated, reducing the total drag from 241.24 counts to 150 counts. In terms of two aerofoil optimisation cases, both Hicks–Henne and FFD geometry parameterisation methods are equivalently effective. The optimisation performance in the NACA 0012 aerofoil case shows dependence on several parameter settings, whereas the optimal solution in the RAE 2822 aerofoil case is insensitive to those settings. Non–unique solutions are found in both 2D cases, which implies that the optimisation problems are ill–posed. For the NACA 0012 wing twist optimisation case, a nearly elliptical wing load distribution is produced using FFD twist parameterisation, and the lift constraint is satisfied. The drag is reduced by approximately one count, which improves the span efficiency by over one percent.

Acknowledgments

References

[1] Bisson, F., Nadarajah, S., and Shi-Dong, D., "Adjoint-based aerodynamic optimization of benchmark problems," *52nd Aerospace Sciences Meeting*, 2014, p. 0412.

[2] Carrier, G., Destarac, D., Dumont, A., Meheut, M., Salah El Din, I., Peter, J., Ben Khelil, S., Brezillon, J., and Pestana, M., "Gradient-based aerodynamic optimization with the elsA software," *52nd Aerospace Sciences Meeting*, 2014, p. 0568.

[3] Lee, C., Koo, D., Telidetzki, K., Buckley, H., Gagnon, H., and Zingg, D. W., "Aerodynamic Shape Optimization of Benchmark Problems Using Jetstream," *53rd AIAA Aerospace Sciences Meeting*, 2015, p. 0262.

[4] Vassberg, J., Harrison, N., Roman, D., and Jameson, A., "A systematic study on the impact of dimensionality for a two-dimensional aerodynamic optimization model problem," *29th AIAA Applied Aerodynamics Conference*, 2011, p. 3176.

[5] Zhang, M., Rizzi, A. W., and Nangia, R. K., "Transonic Airfoils and Wings Design Using Inverse and Direct Methods," *53rd AIAA Aerospace Sciences Meeting*, 2015, p. 1943.

[6] Leifsson, L. T., Koziel, S., Tesfahunegn, Y. A., Hosder, S., and Gramanzini, J.-R., "Application of Physics-Based Surrogate Models to Benchmark Aerodynamic Shape Optimization Problems," *53rd AIAA Aerospace Sciences Meeting*, 2015, p. 0265.

[7] Anderson, G. R., Nemec, M., and Aftosmis, M. J., "Aerodynamic shape optimization benchmarks with error control and automatic parameterization," *53rd AIAA Aerospace Sciences Meeting*, 2015, p. 1719.

[8] Poole, D. J., Allen, C. B., and Rendall, T., "Control point-based aerodynamic shape optimization applied to aiaa adodg test cases," *53rd AIAA Aerospace Sciences Meeting*, 2015, p. 1947.

[9] Poole, D. J., Allen, C. B., and Rendall, T., "Application of control point-based aerodynamic shape optimization to two-dimensional drag minimization," *52nd Aerospace Sciences Meeting*, 2014, p. 0413.

[10] Masters, D. A., Poole, D. J., Taylor, N. J., Rendall, T., and Allen, C. B., "Impact of shape parameterisation on aerodynamic optimisation of benchmark problem," *54th AIAA Aerospace Sciences Meeting*, 2016, p. 1544.

[11] LeDoux, S. T., Vassberg, J. C., Young, D. P., Fugal, S., Kamenetskiy, D., Huffman, W. P., Melvin, R. G., and Smith, M. F., "Study based on the AIAA aerodynamic design optimization discussion group test cases," *AIAA Journal*, Vol. 53, No. 7, 2015, pp. 1910–1935.

[12] Méheut, M., Destarac, D., Ben Khelil, S., Carrier, G., Dumont, A., and Peter, J., "Gradient-Based Single and Multi-points Aerodynamic Optimizations with the elsA Software," *53rd AIAA Aerospace Sciences Meeting*, 2015, p. 0263.

[13] Economon, T. D., Palacios, F., Copeland, S. R., Lukaczyk, T. W., and Alonso, J. J., "SU2: An Open-Source Suite for Multiphysics Simulation and Design," *AIAA Journal*, Vol. 54, No. 3, 2016, pp. 828–846.

[14] Palacios, F., Alonso, J., Duraisamy, K., Colonno, M., Hicken, J., Aranake, A., Campos, A., Copeland, S., Economon, T., Lonkar, A., et al., "Stanford University Unstructured (SU2): an open-source integrated computational environment for multi-physics simulation and design," *51st AIAA Aerospace Sciences Meeting*, 2013, p. 287.

[15] Kuhn, H. and Tucker, A., "Nonlinear programming," *Proceedings of 2nd Berkeley Symposium. Berkeley: University of California Press*, 1951, pp. 481–492.

[16] Karush, W., *Minima of functions of several variables with inequalities as side conditions*, Ph.D. thesis, 1939.

[17] Jameson, A., Schmidt, W., and Turkel, E., "Numerical solution of the Euler equations by finite volume methods using Runge Kutta time stepping schemes," *14th fluid and plasma dynamics conference*, 1981, p. 1259.

American Institute of Aeronautics and Astronautics

[18]Spalart, P. and Allmaras, S., "A one-equation turbulence model for aerodynamic flows," *30th aerospace sciences meeting and exhibit*, 1992, p. 439.

[19]Economon, T. D., Palacios, F., and Alonso, J. J., "A viscous continuous adjoint approach for the design of rotating engineering applications," *21st AIAA Computational Fluid Dynamics Conference*, 2013, p. 2580.

[20]Dwight, R. P., "Robust mesh deformation using the linear elasticity equations," *Computational Fluid Dynamics 2006*, Springer, 2009, pp. 401–406.

[21]Hicks, R. M. and Henne, P. A., "Wing design by numerical optimization," *Journal of Aircraft*, Vol. 15, No. 7, 1978, pp. 407–412.

[22]Sederberg, T. W. and Parry, S. R., "Free-form deformation of solid geometric models," *ACM SIGGRAPH computer graphics*, Vol. 20, No. 4, 1986, pp. 151–160.

[23]Jameson, A., Vassberg, J. C., and Ou, K., "Further studies of airfoils supporting non-unique solutions in transonic flow," *AIAA journal*, Vol. 50, No. 12, 2012, pp. 2865–2881.

[24]Ou, K., Jameson, A., and Vassberg, J. C., "Airfoils supporting non-unique transonic solutions for unsteady viscous flows," *7th AIAA Theoretical Fluid Mechanics Conference*, 2014, p. 2927.

American Institute of Aeronautics and Astronautics